



THE UNIVERSITY *of* EDINBURGH

Edinburgh Research Explorer

## Heat Transfer in Unfrozen and Frozen Porous Media: Experimental Measurement and PoreScale Modelling

**Citation for published version:**

Farahani, MV, Hassanpouryouzband, A, Yang, J & Tohidi, B 2020, 'Heat Transfer in Unfrozen and Frozen Porous Media: Experimental Measurement and PoreScale Modelling', *Water Resources Research*.  
<https://doi.org/10.1029/2020WR027885>

**Digital Object Identifier (DOI):**

[10.1029/2020WR027885](https://doi.org/10.1029/2020WR027885)

**Link:**

[Link to publication record in Edinburgh Research Explorer](#)

**Document Version:**

Publisher's PDF, also known as Version of record

**Published In:**

Water Resources Research

**Publisher Rights Statement:**

©2020. The Authors.

**General rights**

Copyright for the publications made accessible via the Edinburgh Research Explorer is retained by the author(s) and / or other copyright owners and it is a condition of accessing these publications that users recognise and abide by the legal requirements associated with these rights.

**Take down policy**

The University of Edinburgh has made every reasonable effort to ensure that Edinburgh Research Explorer content complies with UK legislation. If you believe that the public display of this file breaches copyright please contact [openaccess@ed.ac.uk](mailto:openaccess@ed.ac.uk) providing details, and we will remove access to the work immediately and investigate your claim.



# Water Resources Research

## RESEARCH ARTICLE

10.1029/2020WR027885

### Key Points:

- A mechanistic study was conducted on pore-scale mechanisms governing heat transfer in porous media at unfrozen and frozen conditions
- Effects of pore and overburden pressures, temperature, and water content on effective thermal conductivity were experimentally investigated
- A pore-scale model was developed to predict effective thermal conductivity using lattice Boltzmann model and a space renormalization method

### Supporting Information:

- Supporting Information S1

### Correspondence to:

J. Yang,  
petjy@hw.ac.uk

### Citation:

Vasheghani Farahani, M., Hassanpouryouzband, A., Yang, J., & Tohidi, B. (2020). Heat transfer in unfrozen and frozen porous media: Experimental measurement and pore-scale modeling. *Water Resources Research*, 56, e2020WR027885. <https://doi.org/10.1029/2020WR027885>

Received 7 MAY 2020




Accepted 9 AUG 2020

Accepted article online 12 AUG 2020

©2020. The Authors.

This is an open access article under the terms of the Creative Commons Attribution License, which permits use, distribution and reproduction in any medium, provided the original work is properly cited.

## Heat Transfer in Unfrozen and Frozen Porous Media: Experimental Measurement and Pore-Scale Modeling

Mehrdad Vasheghani Farahani<sup>1</sup> , Aliakbar Hassanpouryouzband<sup>1,2</sup> , Jinhai Yang<sup>1</sup> , and Bahman Tohidi<sup>1</sup>

<sup>1</sup>Hydrates, Flow Assurance and Phase Equilibria Research Group, Institute of GeoEnergy Engineering, Heriot-Watt University, Edinburgh, UK, <sup>2</sup>School of Geosciences, University of Edinburgh, Grant Institute, Edinburgh, UK

**Abstract** In this work, we conducted a mechanistic study on pore-scale mechanisms controlling heat transfer in partially saturated porous media at unfrozen and frozen conditions. Experimental measurement of effective thermal conductivity (ETC) of simulated partially saturated sediments was carried out to explore the effect of different parameters including pore and overburden pressures, temperature, and water/ice saturation on the pore-scale mechanisms governing heat transfer in multiphase porous media. The experimental measurements show that the heat transfer is a complex phenomenon affected by several important pore-scale mechanisms such as particle-particle conduction and particle-fluid-particle conduction, which are governed by water content and distribution, packing structure, wettability characteristics of grains, coordination number, and physical contact among sediment particle. A numerical model was also developed for prediction of ETC using free-energy lattice Boltzmann model and a space renormalization method. The model predictions were in good agreement with the experimental data, showing that the model is able to reliably estimate ETC with average relative deviations of less than 10%, as it appropriately incorporates the pore-scale mechanisms influencing ETC. The numerical model predictions were also compared with those of six predictive models available in the literature, and root-mean-square errors were calculated to assess its accuracy against the existing models.

## 1. Introduction

Effective thermal conductivity (ETC) is a key physical property of heat transport in porous media. ETC studies of dry and fluid-saturated porous media are of utmost importance in a variety of geotechnical, geophysical, and geoenvironmental applications, such as underground transmission lines, geothermal energy resources, solar thermal storage facilities, radioactive waste disposal, geological CO<sub>2</sub> sequestration, and methane recovery from gas hydrate-bearing sediments (Abdulagatova et al., 2009; Li et al., 2013; van Antwerpen et al., 2010). In environmental science context, accurate quantification of ETC for soil and shallow unfrozen/frozen marine sediments could deliver essential information regarding the seafloor stability assessment, sedimentation, submarine slide formation, and global climate change. In particular, ETC plays a key role in geothermal energy engineering (e.g., ground source heat pumps, borehole thermal energy storage, and geothermal heated bridge/pavement) as it affects the kinetic behavior of working fluid temperature, which is essential for efficient design of the processes in this chain. A faster charging and discharging rate could be achieved by selecting a geological medium with higher ETC, while geological media with lower ETC values could be chosen for longer maintenance of the working fluid temperature. Therefore, reliable ETC values for soil are of particular importance for geothermal applications (Zhang & Wang, 2017). ETC is even more crucial in the study of the impact of environmental changes on stability of the natural gas hydrate-bearing sediments and evaluation of the the exploitation associated risks (Waite et al., 2009). For instance, dissociation of stable hydrate-bearing layers could be derived by withdrawal of deep, warm fluids via a conductor that travels across these layers, weakening seafloor sediment stability (Freij-Ayoub et al., 2007; Hovland & Gudmestad, 2001). Here, higher ETC could increase the risk. In contrast, ETC is required to be high enough for choosing materials used in nuclear waste disposal as it results in more efficient cooling and uniform temperature distribution and reduces thermally induced stress which, in turn, improves fatigue properties (Pinheiro et al., 2011). Returning to geological importance of ETC for

soils, integrity of caprocks for stored CO<sub>2</sub> could possibly be weakened by thermal stress caused by injected fluid that is also highly dependent on ETC of caprock (Gor et al., 2013).

Thermal properties of porous media depend upon not only the intrinsic thermal properties and volume fraction of each constituent but also pressure, temperature, porosity, and packing structure (Cortes et al., 2009). Focused on sediments, the other influencing factors include mineralogy, packing structure and gradation, and interparticle physical contact among grains (Dong et al., 2015; Ghanbarian & Daigle, 2016; Sadeghi et al., 2018; Zhang & Wang, 2017). At temperatures below the freezing point, transformation of water to ice (with lower density and higher intrinsic thermal conductivity) together with the presence of unfrozen water may even add more complexities in the system.

Experimental studies have been conducted so far to determine ETC of fully and partially water saturated soil samples at unfrozen conditions. The results indicate that ETC of a given soil is largely influenced by quartz and water contents since quartz has the highest thermal conductivity among all the soil minerals and thermal conductivity of air is markedly lower than that of water (Barry-Macaulay et al., 2013; Côté & Konrad, 2005; Lu et al., 2019; Nikolaev et al., 2013; Tarnawski et al., 2009; Venuleo et al., 2016; Zhang et al., 2015; Zhao et al., 2019). There are also a number of work investigating the effect of the soil mineral components, particle size, shape, and gradation on its ETC (Campbell et al., 1994; Chen, 2008; Côté et al., 2011). Complexities associated with the presence of clay or other binders were also explored in laboratory (Abuel-Naga et al., 2008, 2009; de Zárate et al., 2010; Yu et al., 2016). Clay appears to significantly improve the heat conduction by cementing the solid grains and reducing the thermal contact resistance (TCR). It was also found that ETC slightly depends on the temperature (Campbell et al., 1994; Hiraiwa & Kasubuchi, 2000; Liu et al., 2011; Lu et al., 2007). Similarly, studies were also conducted to determine the soil thermal properties at frozen conditions, mainly aiming at understanding the effect of climate change, seasonal freezing-thawing processes, and human activities on thermal response in permafrost regions (Domine et al., 2016; Du et al., 2020; He et al., 2018; Kojima et al., 2018; Overduin et al., 2006; Putkonen, 2003; Wang et al., 2017; Zhao & Si, 2019). Despite considerable work conducted so far, it is still imperative to conduct experimental studies, particularly at pore scale, to shed light on the mechanisms controlling the heat transfer in unsaturated porous media and more importantly understand their interdependencies.

Numerous predictive models have been proposed to estimate ETC of porous materials; however, a unified model or prediction procedure with universal applicability is yet to be developed (Dong et al., 2015). Depending on their principles and assumptions, available predictive models could be categorized into (i) mixing models, which determine ETC by combining the intrinsic thermal conductivity values of the coexisting constituents, typically as a function of volume fraction (Abdulagatova et al., 2009); (ii) empirical models, which build a relationship between ETC and volumetric water content, porosity, and type of the sediment grains by normalizing ETC over the difference between fully saturated and dry state ETC values; (iii) mathematical models, which are adopted from predictive models used to determine other physical properties of composite materials, such as electrical conductivity and hydraulic conductivity; (iv) volume fraction models, which estimate ETC with respect to level of their solid volume fraction (low, medium, and high volume fraction materials); (v) packing structure models, which are developed based on the different packing structures of spheres such as simple cubic, body centered cubic, and face centered cubic; and (vi) pressure-dependent models, which treat the sediment as a standard unit cell containing two contacting particles and take the effect of the compressive pressure into account in order to capture the effect of TCR between grains as the contact area and TCR was shown to markedly control the heat transfer through a porous medium (Garrett & Ban, 2011; Yun & Santamarina, 2007). These predictive models were critically reviewed elsewhere (Abdulagatova et al., 2009; Dong et al., 2015; Zhang & Wang, 2017).

Available predictive models are based on either based on empirical fits to experimental data or conceptualization of the multiphase porous system as a certain combination of series/parallel solid, air, and/or water blocks in a representative elementary volume. These models cannot realistically account for pore-scale mechanisms (fluid-fluid and rock-fluid interactions, pore-scale habit of each coexisting phase, and changes in the thermal state) controlling the heat transfer. Therefore, they need adjusting parameters whose values are usually a priori unknown, making the models dependent on the experimental data, and may accordingly restrict their applications (Sadeghi et al., 2018). In fact, a more comprehensive insight into these pore-scale mechanisms is required for further development of predictive models. Efforts have been made to account for

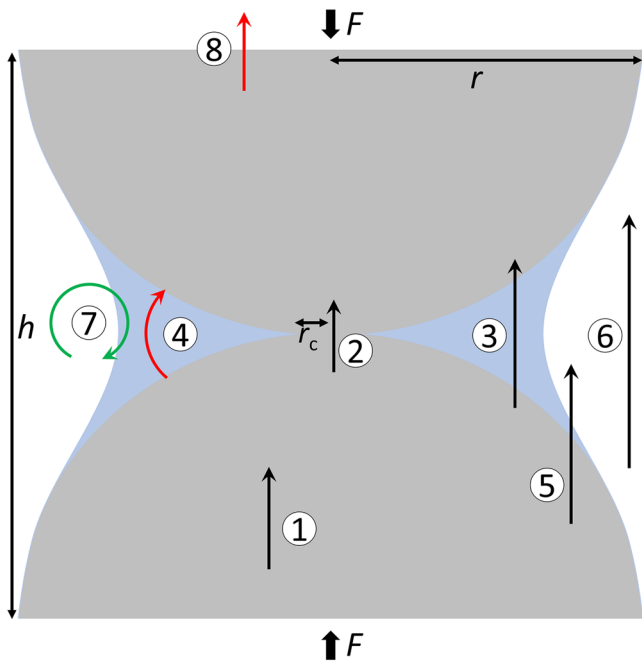


**Figure 1.** Particle-level heat transfer mechanisms for a standard unit cell: (1) particle conduction, (2) contact conduction, (3) particle-fluid-particle conduction, (4) particle-particle radiation, (5) particle-fluid conduction, (6) pore fluid conduction, (7) pore fluid convection, and (8) radiation into the surrounding medium.

these mechanisms by developing predictive models having physically meaningful parameters. One popular approach is to implement the pore-scale mechanisms into the unit cell. There are a number of models developed for predicting ETC of dry particulate beds in which a contact equation is employed to account for TCR (Bahrami et al., 2006; Dai et al., 2019; Garrett & Ban, 2011; Mo & Ban, 2017; Slavin et al., 2000; Weidenfeld et al., 2004). Some other unit cell-based models take into consideration the effect of the water content, hence applicable for unsaturated soils (Chu et al., 2019; Corasaniti & Gori, 2017; Ewing & Horton, 2007; Gori & Corasaniti, 2013; Likos, 2015). Use of such models is computationally affordable; however, their accuracy and application strongly depend on how they incorporate the pore-scale associated phenomena. More sophisticated approaches such as discrete element method and boundary element method have been also adopted recently to study the heat transfer in soil and establish more detailed predictive models (El Shamy et al., 2013; Feng et al., 2008; Yun & Evans, 2010; Zhou et al., 2007).

In this study, we report experimental measurements of ETC of simulated partially saturated sediments. Four sets of experiment were conducted to investigate the effect of pore pressure, overburden pressure, temperature, and degree of water/ice saturation on the pore-scale associated phenomena controlling heat conduction in a multiphase porous system. We also developed a numerical model for prediction of ETC, where free-energy lattice Boltzmann model (LBM) is first utilized to set the coexisting phases of water and gas ( $N_2$ ) at equilibrium in a cubic domain, composed of a 3-D standard unit cell surrounded by an annular region filled with the gas. ETC of the cubic domain is then calculated via applying a space renormalization method on the system at equilibrium conditions. ETC of the standard unit cell is simply calculated by deducting the thermal conductivity of the annular region from ETC of the cubic domain based on the weighted averaging method. The model is able to account for several pore-scale mechanisms simultaneously, having more accurate predictions than the other existing models available in the literature.

ETC of the standard unit cell is simply calculated by deducting the thermal conductivity of the annular region from ETC of the cubic domain based on the weighted averaging method. The model is able to account for several pore-scale mechanisms simultaneously, having more accurate predictions than the other existing models available in the literature.

## 2. Background

Heat transfer in granular materials is controlled by several particle-level mechanisms: (1) conduction within the mineral, (2) particle-particle conduction through the contact area, (3) particle-fluid-particle conduction, which is of particular relevance in partially saturated sediments, (4) radiation at interparticle contacts, (5) particle-fluid-particle conduction, (6) conduction in pore fluid, (7) convection in pore fluid, and (8) radiation from the particle surface into the surrounding medium (Yun & Santamarina, 2007). Figure 1 schematically illustrates these mechanisms for a cylindrical standard unit cell. Heat transfer could be considered conductive at naturally occurring porous sediments, particularly in fine sands and clays at low temperatures given negligible relative contribution of free convective and radiative mechanisms (Waite et al., 2009).

There are two types of thermal conductivity measurements including steady state methods and unsteady state methods. In this work, we employed transient hot wire method, which is an unsteady state procedure extensively used to measure the thermal conductivity of intact and reconstituted porous substances in a wide range of temperatures. In this method, thermal conductivity is obtained by a variation of the line source test method using a needle probe, which is required to have a large length to diameter ratio to comply with the line-source solution assumption, that is, an infinitely long, infinitely thin heating source (ASTM D5334-14, 2014). The needle probe consists of a heating wire, representing a perfect line source and a temperature sensor for measuring the temperature. The probe is inserted into the specimen, certain current and voltage are applied to the probe, and the temperature rise with time is recorded over a period of time. Thermal conductivity is obtained via analyzing the temperature time series data during the heating cycle (ASTM D5334-14, 2014).

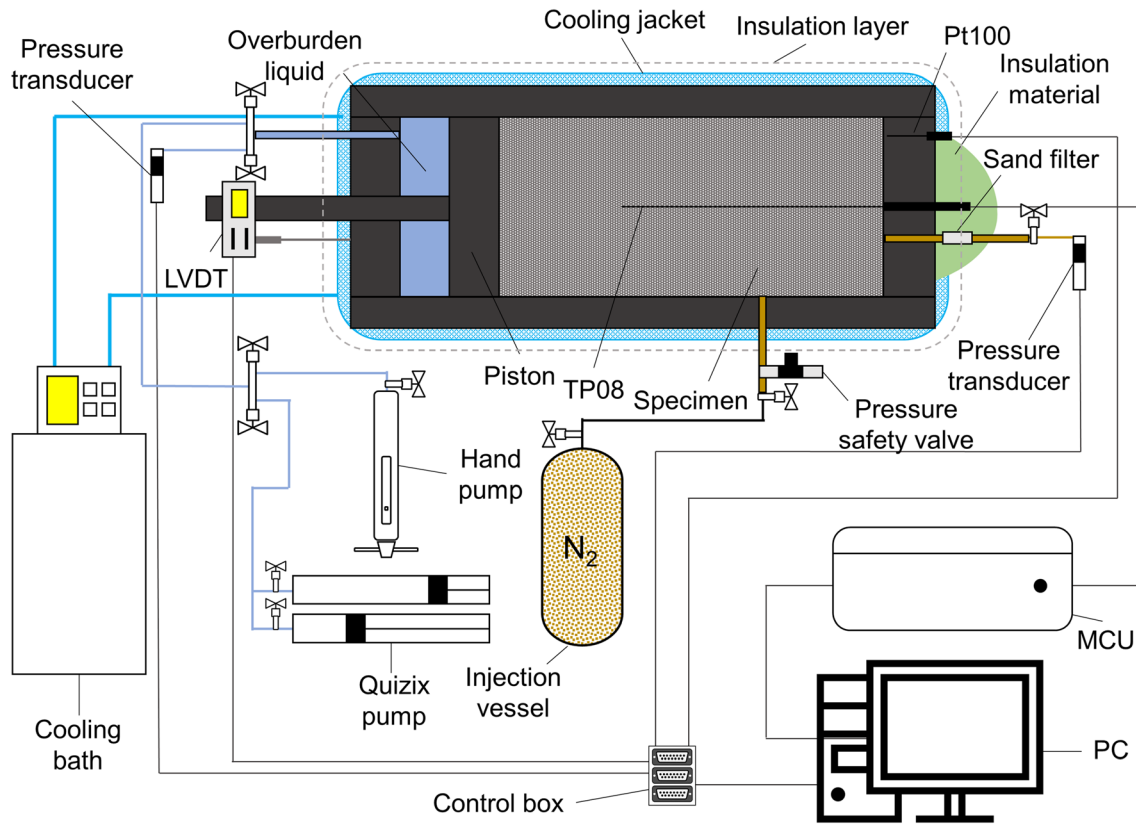


Figure 2. Schematic diagram of the high-pressure apparatus.

In contrast with steady state methods, transient hot wire method could be conducted with substantial less required time for measurements (Abdel-Wahed et al., 1978; Jongwon et al., 2019). Moreover, the sample size is not critical as long as the diameter of the medium surrounding the needle is 10 times the diameter of the thermal needle probe (ASTM D5334-14, 2014). At a constant amount of heat flux, the temperature response of an ideal (zero mass) heater over a period of time could be expressed by Equation 1:

$$\Delta T = -\frac{Q}{4\pi\lambda} Ei\left(\frac{-r^2}{4\kappa t}\right) \quad 0 < t < t_1 \quad (1)$$

where  $t$ ,  $\Delta T$ ,  $Q$ ,  $r$ ,  $\kappa$ ,  $\lambda$ ,  $Ei$ , and  $t_1$  stand for the measuring time, temperature change, applied heat per unit length of heater, distance from the heated needle, thermal diffusivity, thermal conductivity, exponential integral, and heating time, respectively (ASTM D5334-14, 2014). The exponential integral in Equation 1 could be approximated by the most significant terms of its series expansion, resulting in Equation 2:

$$\Delta T \cong \frac{Q}{4\pi\lambda} \ln(t) \quad 0 < t < t_1 \quad (2)$$

Therefore,  $\lambda$  could be calculated from the slope of the best fit line relating  $\Delta T$  to  $\ln(t)$ . When analyzing the data, care must be taken to exclude the early and late portions of the test, representing transient conditions where the measurements were strongly influenced by terms ignored in Equation 2 and boundary conditions where the measurements were affected by the external boundary of the system, respectively.

### 3. Experimental Section

#### 3.1. Experimental Setup

ETC measurements were conducted using a 316 stainless steel cylindrical cell setup, which is schematically illustrated in Figure 2. The setup consists of a high-pressure stainless steel cell with an inner diameter of

75 mm and inner length of 200 mm, satisfying the minimum length and diameter required according to ASTM standard (see ASTM D5334-14 standard, ASTM D5334-14, 2014). The setup can be placed horizontally or vertically on a pivot. An integral cooling jacket was fitted around the cell and connected to a cryostat (Grant LTC) to maintain the desired isothermal conditions during measurements. A calibrated platinum-resistance thermometer (Pt100, supplied by TC Ltd.) with an accuracy of better than  $\pm 0.1$  K was also coated in the cell to measure its temperature. A movable piston driven by hydraulic pressure was placed at one end of the cell, used for compacting sediments at a desired overburden pressure. The overburden pressure was achieved by fluid injection behind the piston using a Quizix pump with dual cylinders (SP-5200, Vindum Engineering Inc., United States) and measured using a calibrated Druck pressure transducer with an accuracy of  $\pm 0.05$  MPa. A linear variable differential transmitter is mounted on the piston rod to determine its position, which enables us to compute the instantaneous sample volume, hence the porosity of the system. There were two ports at the fixed endcap, one for the gas introduction and the other connected to another calibrated Druck pressure transducer for measuring the pore pressure. It should be noted that we inserted a fine mesh screen in the discharge point of each port to avoid intrusion of the sand particles and baffle the gas stream during injection to retain the initial homogeneous water distribution. The pressure and temperature data together with the piston movement were continuously monitored at regular time intervals, collected using a data acquisition module, and recorded on a PC with a LabVIEW software (National Instruments).

The thermal conductivity measurements were made using a calibrated purpose-built needle probe (TP08, Hukseflux, Netherlands), which can accurately measure the thermal conductivity at elevated pressures in compliance with the ASTM D5334-14 standard. In TP08, the reference junction of the thermocouple is located in the base. Hence, before loading the cell with the test specimen, the probe is mounted on the fixed endcap and its base fully covered with an insulation material to minimize the influence of heat exchange with the laboratory environment on the thermal conductivity measurements. The thermal conductivity data were all recorded in a measurement and control unit connected to the PC.

### 3.2. Materials

Research-grade  $N_2$  (purity 99.995 vol.%) was supplied by BOC Ltd. Deionized water generated by an integral water purification system (ELGA DV 25) was used throughout the experiments. The simulated sediment used in this study was a well-characterized silica sand from Fife, Scotland (grain density:  $2.64 \text{ g/cm}^3$ , mean size:  $257 \text{ }\mu\text{m}$ , and specific area:  $0.059 \text{ m}^2/\text{cm}^3$ ); a detailed analysis of which could be found elsewhere (Hassanpouryouzband, Yang, Okwananke, et al., 2019; Hassanpouryouzband, Yang, Tohidi, et al., 2019).

### 3.3. Procedure

#### 3.3.1. Sample Preparation and Configuration

Each test specimen was made by mixing the silica sand and deionized water at a predetermined mass ratio with respect to the desired water saturation. The mixture was loaded within the cell that was washed, dried, positioned vertically, and equipped with the thermal conductivity probe instrumentation. While loading, the specimen was regularly tamped using a purpose-built pestle to attain uniform compaction and ensure full contact with the probe. After the specimen reached the desired height, the other endcap was installed, and the cell was rotated back to the horizontal position. The bath temperature was also set to the target temperature, and the cell was vacuumed. A hydraulic pressure was then applied behind the piston using the Quizix pump to further compact the sediment at the desired overburden pressure. The system was left for 24 hr at this condition to reach thermal equilibrium.  $N_2$  was then injected into the cell until the pore pressure reaches the desired value while maintaining the effective overburden pressure. The system was left at this condition until the pressure and temperature of the system become stable and no piston movement is observed. Finally, the specimen underwent the ETC measurement.

#### 3.3.2. Thermal Conductivity Measurements

Four sets of experiment were carried out in order to explore the effect of the system temperature ( $T$ ), pore pressure ( $P_{\text{Pore}}$ ), effective overburden pressure ( $P_{\text{OB, eff.}}$ ), and water content ( $\theta_w$ ) on ETC of sediments. The experimental sets are summarized in Table 1. As observed, for each individual parameter, a base value was considered:  $T = 0.5^\circ\text{C}$ ,  $P_{\text{Pore}} = 3.45 \text{ MPa}$ ,  $\theta_w = 12.6 \text{ wt.}\%$  ( $S_w \approx 55\%$ ), and  $P_{\text{OB, eff.}} = 3.45 \text{ MPa}$ . Each experimental set was carried out by changing two parameters while keeping the other two at their base

**Table 1**  
Summary of the Physical Parameters Considered for Each Experimental Set

Set	$T$ (°C)	$P_{\text{Pore}}$ (MPa)	$S_w$ (–)	$P_{\text{OB, eff.}}$ (MPa)
1	Base value	2.76, 8.27, 13.79	Base value	1.38, 4.14, 6.89, 9.65
2	–10, –5, 0.5, 5, 10	Base value	Base value	1.38, 4.14, 6.89, 9.65
3	–10, –5, 0.5, 5, 10	1.38, 4.14, 6.89, 9.65, 12.41, 15.17, 17.93	Base value	Base value
4	Base value	1.38, 4.14, 6.89, 9.65, 12.41, 15.17	0.00, 0.09, 0.31, 0.65, 1.00	Base value

values. This enabled us to investigate the effect of each individual parameter on ETC as well as capture their interdependencies.

Most of ETC measurements were repeated for the elimination of the experimental data contingencies. Moreover, at frozen conditions, the total heat to the specimen was reduced to impose a smaller temperature gradient in order to minimize the possibility of fluid convection and phase change around the needle probe. After completion of ETC measurements, three sediment samples were taken from different sections in the cell and their water saturation was measured to check the homogeneity of the system. ETC was then obtained by analyzing the experimental data according to Equation 2.

#### 4. Numerical Modeling

A numerical model was developed to predict ETC of partially saturated sediments under applied overburden pressure. The model uses a 3-D standard unit cell containing two monosized touching hemispheres in contact with the coexisting fluids, that is, water/ice and gas ( $N_2$ ) at equilibrium conditions. The whole computational procedure could be divided into three steps:

##### 4.1. Preprocessing

To begin with, a 3-D standard unit cell with  $2r$  by  $2r$  square cross-section area ( $r$  stands for the hemisphere radius) and  $h$  in height, containing two perfectly round hemispheres with a flat Hertzian contact interface, is constructed (Figure 1). In this study, the simple cubic packing configuration was identified to be appropriate based on the porosity range of our specimens (Siu & Lee, 2000). The contact radius,  $r_c$ , is calculated by the Hertz contact equation (Johnson, 1987):

$$r_c = \sqrt[3]{\frac{3Fr(1 - \nu^2)}{4E}} \quad (3)$$

where  $F$ ,  $\nu$ , and  $E$  are the contact force, Poisson's ratio, and Young's modulus. This makes it possible to account for the heat flow through the sphere-contact-sphere and accordingly incorporate TCR as a function of the effective overburden pressure, which could be considered as a distinguishing feature of our numerical model.

According to Figure 1, the half spheres are in contact with static fluids filling the rest of unit cell. We employed free-energy LBM to set the two phases of water and gas ( $N_2$ ). LBM is a computational fluid dynamics solver based on mesoscopic kinetic equations, which could be utilized to study fluid flow problems (Krüger et al., 2017). LBM has proven to be a powerful tool for solving problems at different length and time scales owing to its advantages in numerical simulation of single-phase and multiphase fluid flows in pore scale (Bakhshian et al., 2019; Chen et al., 2019; Norouzi et al. 2019; Zhang et al., 2019), particularly in complex geometries such as porous media (Bakhshian & Sahimi, 2016; Vasheghani Farahani et al., 2019; Vora & Dugan, 2019). Free-energy LBM as an option for simulating multiphase and multicomponent fluid flow is able to appropriately account for fluid-fluid interfacial tensions and solid surface contact angles. The free-energy LBM algorithm is implemented in OpenLB (<http://www.openlb.net>), an Open Source numerical framework for lattice Boltzmann simulations (Krause et al., 2019). Here, we briefly describe the free-energy LBM for a binary system in which the fluid-fluid surface tension and fluid-solid surface interactions (contact angle) could be derived and independently controlled. Further details of the algorithm implemented in OpenLB could be referred in the literature (Sadullah et al., 2018; Semperebon et al., 2016; Wöhrwag et al., 2018).

A free-energy functional that models a system with two fluid components with concentration fractions of  $C_1$  and  $C_2$  ( $C_1 + C_2 = 1$ ) could be expressed by (Semperebon et al., 2016):

$$F = \int_{\Omega} \left[ \frac{\kappa_1 + \kappa_2}{2} C_1^2 (1 - C_1)^2 + \frac{\alpha^2 (\kappa_1 + \kappa_2)}{2} (\nabla C_1)^2 \right] dV - \int_{\partial\Omega} (h_1 C_1 + h_2 C_2) dS \quad (4)$$

where  $\Omega$  is the system volume and  $\alpha$  and  $\kappa$  are two tuning parameters for the interfacial width and surface tension. The interfacial width is expressed by  $\alpha$  (typically chosen to be 1.0) and the surface tension ( $\gamma_{12}$ ) by (Sadullah et al., 2018)

$$\gamma_{12} = \frac{\alpha(\kappa_1 + \kappa_2)}{6} \quad (5)$$

The  $h_i$  parameters in Equation 4 make it possible to quantify the fluid-solid surface energies, hence the contact angle of fluid 1 on a solid surface in the presence of fluid 2 ( $\theta_{12}$ ), which could be given by (Sadullah et al., 2018)

$$\theta_{12} = \cos^{-1} \left( \frac{\gamma_{s1} - \gamma_{s2}}{\gamma_{12}} \right) \quad (6)$$

where  $\gamma_{si}$  is the surface tension between the fluid phase  $i$  and solid surface, which essentially includes contributions from the both phases,  $i$  and  $j$ , and could be expressed by (Sadullah et al., 2018)

$$\gamma_{si} = \left( \frac{\alpha\kappa_i}{12} - \frac{h_i}{2} - \frac{4h_i + \kappa_i\alpha}{12} \sqrt{1 + \frac{4h_i}{\alpha\kappa_i}} \right) + \left( \frac{\alpha\kappa_j}{12} - \frac{h_j}{2} + \frac{4h_j - \kappa_j\alpha}{12} \sqrt{1 - \frac{4h_j}{\alpha\kappa_j}} \right) \quad (7)$$

Therefore, the contact angle could be given by the following expression as a function of  $\kappa_1$ ,  $\kappa_2$ ,  $h_1$ , and  $h_2$  (Semperebon et al., 2016):

$$\theta_{12} = \cos^{-1} \left( \frac{(\alpha\kappa_2 + 4h_2)^{3/2} - (\alpha\kappa_2 - 4h_2)^{3/2}}{2(\kappa_1 + \kappa_2)\sqrt{\alpha\kappa_2}} - \frac{(\alpha\kappa_1 + 4h_1)^{3/2} - (\alpha\kappa_1 - 4h_1)^{3/2}}{2(\kappa_1 + \kappa_2)\sqrt{\alpha\kappa_1}} \right) \quad (8)$$

Variable transformation from  $C_1$  and  $C_2$  to two equivalent order parameters of  $\rho = C_1 + C_2$  and  $\phi = C_1 - C_2$  could be applied to satisfy the hard constraint of  $C_1 + C_2 = 1$ . The continuum equations of motion of the system are the continuity, Navier-Stokes, and Cahn-Hilliard equations (Wöhrwag et al., 2018):

$$\begin{cases} \partial_t \rho + \nabla \cdot (\rho \mathbf{v}) = 0 \\ \partial_t (\rho \mathbf{v}) + \nabla \cdot (\rho \mathbf{v} \otimes \mathbf{v}) = -\nabla \cdot \mathbf{P} + \nabla \cdot [\eta (\nabla \mathbf{v} + \nabla \mathbf{v}^T)] \\ \partial_t \phi + \nabla \cdot (\phi \mathbf{v}) = M_{\phi} \nabla^2 \mu_{\phi} \end{cases} \quad (9)$$

where  $\mathbf{v}$ ,  $\mathbf{P}$ , and  $\eta$  are the fluid velocity, fluid dynamic viscosity (which generally depends on the local order parameter  $\phi$ ), and pressure tensor, respectively. The thermodynamic properties of the system described in the free-energy model (Equation 4) enter the equations of motion via the chemical potential ( $\mu_{\phi}$ ) and the pressure tensor. The lattice Boltzmann algorithm described by Semperebon et al. (2016) can be implemented to solve the equations of motion. For a binary system, two distribution functions,  $f_i(\mathbf{x}, t)$  and  $g_i(\mathbf{x}, t)$ , corresponding to the density of the fluid  $\rho$  and the order parameter  $\phi$  are required. The physical variables could be related to the distribution functions by

$$\begin{cases} \rho(\mathbf{x}, t) = \sum_i f_i(\mathbf{x}, t) \\ \rho(\mathbf{x}, t) \mathbf{v}_{\beta}(\mathbf{x}, t) = \sum_i f_i(\mathbf{x}, t) e_{i\beta} \\ \phi(\mathbf{x}, t) = \sum_i g_i(\mathbf{x}, t) \end{cases} \quad (10)$$

The quantities  $e_{i\beta}$  correspond to the standard lattice velocities in the lattice Boltzmann (LB) method. The lattice structure we utilized here is D3Q19 with 19 velocities in three dimensions. A standard BGK (Bhatnagar-Gross-Krook) collision operator could be used for the collision step:



**Table 2**  
Free-Energy LB Simulation Parameters

No.	Parameter	Value (in LB units)
1	$\alpha$	1.0
2	$\kappa_1$	0.005
3	$\kappa_2$	0.005
4	$\Gamma_\phi$	10
5	$h_1$	-0.001086
6	$h_2$	0.001086

$$\begin{cases} f_i^*(\mathbf{x}, t) = f_i(\mathbf{x}, t) - \frac{\Delta t}{\tau} [f_i(\mathbf{x}, t) - f_i^{eq}(\mathbf{x}, t)] \\ g_i^*(\mathbf{x}, t) = g_i(\mathbf{x}, t) - \frac{\Delta t}{\tau_\phi} [g_i(\mathbf{x}, t) - g_i^{eq}(\mathbf{x}, t)] \end{cases} \quad (11)$$

For the streaming step, we have

$$\begin{cases} f(\mathbf{x} + \mathbf{e}_i \Delta t, t + \Delta t) = f_i^*(\mathbf{x}, t) \\ g(\mathbf{x} + \mathbf{e}_i \Delta t, t + \Delta t) = g_i^*(\mathbf{x}, t) \end{cases} \quad (12)$$

where  $\Delta t$  stands for the lattice time step and  $f_i^{eq}(\mathbf{x}, t)$  and  $g_i^{eq}(\mathbf{x}, t)$  are the local distribution functions. The relaxation times  $\tau$  and  $\tau_\phi$  are related to the transport coefficient in the hydrodynamic equations,  $\eta$  and  $M_\phi$ :

$$\begin{cases} \eta = \rho c_s^2 \left( \tau - \frac{\Delta t}{2} \right) \\ M_\phi = \Gamma_\phi \left( \tau_\phi - \frac{\Delta t}{2} \right) \end{cases} \quad (13)$$

in which  $\Gamma_\phi$  is a tunable parameter that appears in the equilibrium distribution. The simulation parameters are tabulated in Table 2.

The LB simulation starts with setting up the geometry of the unit cell, followed by creating and initializing mesh with an optimum resolution in terms of the stabilization of the results and computational cost. This consists of classifying them with material numbers according to their type (1: fluid nodes, 2: solid boundary nodes, and 0: inner solid nodes). Fluid nodes are divided into two lattices, and their initial spatial distribution is specified based on the desired saturation. The lattice dynamics are then set for all nodes based on their material number, and the collision model along with the boundary behavior is characterized. The next step is the main LB loop where the collision and streaming are conducted, followed by the lattice coupling and boundary condition treatment in order to account for the fluid-fluid and solid-fluid interactions, respectively. The spatial distribution of the phases at equilibrium conditions are finally extracted to be used for the next step. If necessary, the volume treatment due to the expansion of the liquid phase at subzero temperatures is also performed.

#### 4.2. Processing

As previously mentioned, we apply a 3-D space renormalization technique to predict ETC of partially saturated sediments. Similar technique has been applied to calculate ETC of tetrahydrofuran hydrate-bearing sands based on 2-D pictures taken by a digital electron microscope and shown to have strong stability and fault tolerance (Huang & Fan, 2005). In this method, a given volume is partitioned into several blocks, each with its own initial property. Based on certain rules, the adjoining eight blocks are considered as a renormalization group to form a new block. The process is repeated until the final block is obtained. We consider the following assumptions to obtain ETC: (i) heat flows in one direction (see Figure 3), (ii) thermal conductivity of blocks containing two phases is averaged based on their volume fractions, (iii) conductive heat resistance is analogous to electrical resistance, and (iv) heat transfer via convection and radiation mechanisms is ignored given their negligible contribution compared with the conduction mechanism (see Cortes et al., 2009).

According to Huang and Fan (2005), a four-block renormalization group (2-D) could be treated as a combination of eight heat conductors (or resistors) on the basis of the analogy between conductive heat transfer and electrical conduction. Similarly, as can be seen in Figure 3, the analogy between conductive heat transfer and electrical conduction enables us to treat each eight-block renormalization group as a combination of 20 heat conductors. The resistances of these heat conductors are

$$\begin{aligned} R_1 &= \frac{1}{2k_A} & R_2 &= \frac{1}{2k_C} & R_3 &= \frac{1}{2k_D} & R_4 &= \frac{1}{2k_B} \\ R_5 &= \frac{1}{2k_A} + \frac{1}{2k_B} & R_6 &= \frac{1}{2k_A} + \frac{1}{2k_C} & R_7 &= \frac{1}{2k_C} + \frac{1}{2k_D} & R_8 &= \frac{1}{2k_B} + \frac{1}{2k_D} \end{aligned}$$

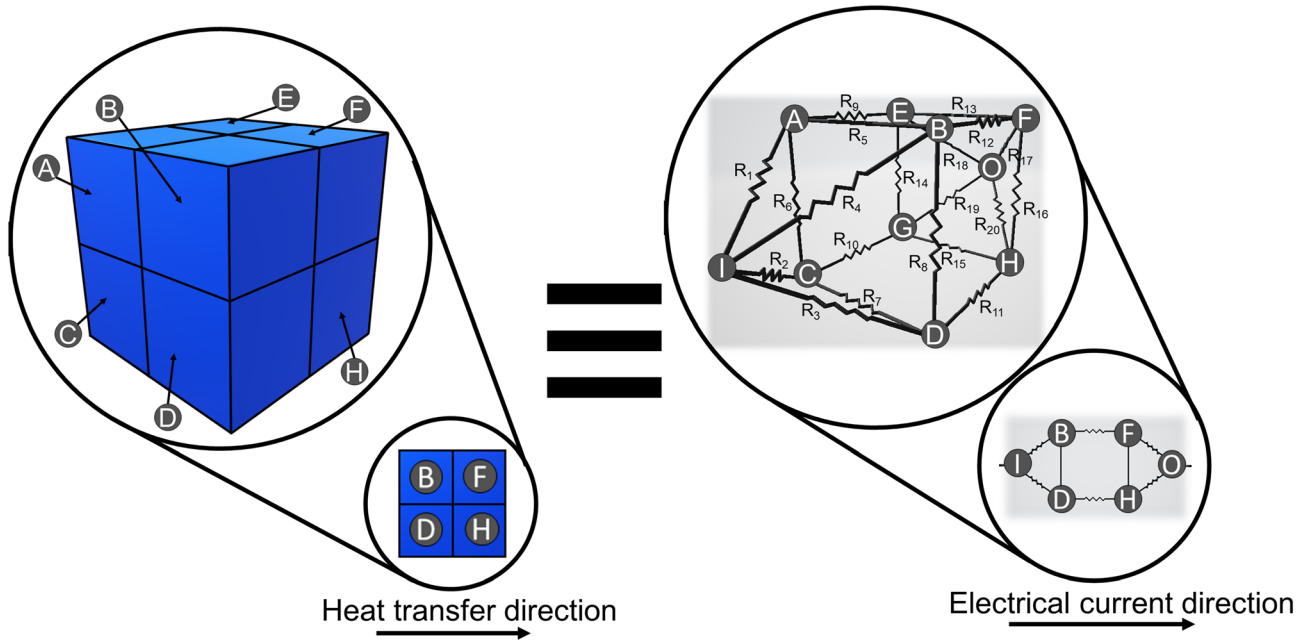


Figure 3. Equivalent heat resistance distribution of eight adjoining blocks.

$$\begin{aligned}
 R_9 &= \frac{1}{2k_A} + \frac{1}{2k_E} & R_{10} &= \frac{1}{2k_C} + \frac{1}{2k_G} & R_{11} &= \frac{1}{2k_D} + \frac{1}{2k_H} & R_{12} &= \frac{1}{2k_B} + \frac{1}{2k_F} \\
 R_{13} &= \frac{1}{2k_E} + \frac{1}{2k_F} & R_{14} &= \frac{1}{2k_E} + \frac{1}{2k_G} & R_{15} &= \frac{1}{2k_G} + \frac{1}{2k_H} & R_{16} &= \frac{1}{2k_F} + \frac{1}{2k_H} \\
 R_{17} &= \frac{1}{2k_F} & R_{18} &= \frac{1}{2k_E} & R_{19} &= \frac{1}{2k_G} & R_{20} &= \frac{1}{2k_H}
 \end{aligned} \tag{14}$$

where  $k$  stands for thermal conductivity and subscripts refer to the adjoining blocks, as shown in Figure 3. The equivalent heat resistance and accordingly the equivalent thermal conductivity could be obtained for each renormalization group by applying Kirchhoff's current law for each individual node (see supporting information). Therefore, this is considered as the core rule of the renormalization process. In addition, it could be concluded that “ $n$ ” stages of the renormalization is required to be conducted on a cubic domain with  $8^n$  ( $2^n \times 2^n \times 2^n$ ) blocks, which necessitates the LB simulation to be performed on a cubic domain with the size of  $(2^n)^3$ . In fact, the parameter  $n$  is a nonnegative integer that determines the number of stages required for the renormalization process and essentially controls the resolution.

The LB simulation results at the preprocessing step consist of the status of each voxel (grain, water, or  $N_2$ ) at equilibrium conditions. Therefore, the simulation domain is already partitioned and labeled. In this step, we assign the thermal conductivity of each individual voxel according to its label and implement the renormalization program in order to obtain the equivalent heat resistance. The thermal conductivity of the voxels located in the fluid-fluid interface is calculated by taking an arithmetic saturation-based average of thermal conductivities of water and  $N_2$ .

It should be noted that we used the thermal conductivity data available in our in-house software for water/ice and nitrogen (Hassanpouryouzband et al., 2018; Hassanpouryouzband, Farahani, et al., 2019). The intrinsic thermal conductivity of sand particles was also obtained by running the numerical model for a case with parameters ( $T$ ,  $P_{\text{Pore}}$ ,  $P_{\text{OB, eff}}$ , and  $\theta_w$ ) set as base values and comparing the predicted ETC with the experimental result, similar to the approach applied by Huang and Fan (2005). By employing this method, the thermal conductivity of sand was obtained as 6.86 W/m.K. The expansion of water due to transformation from liquid to solid (ice) at temperatures below the freezing point is accommodated as follows:

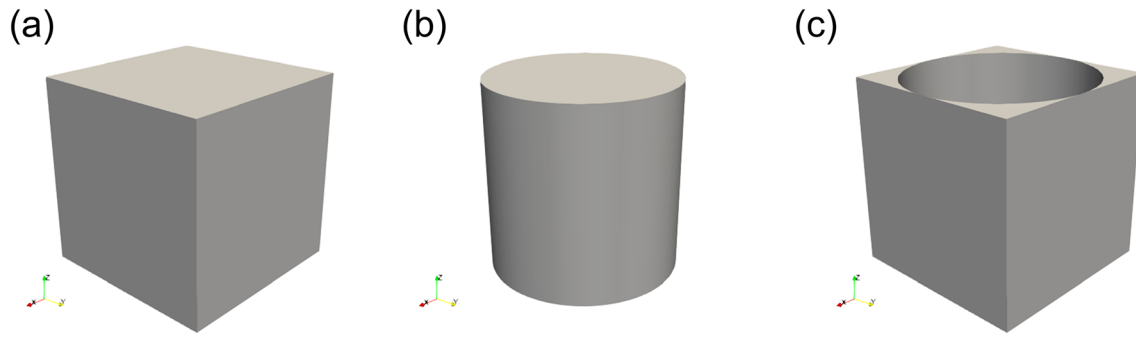


**Figure 4.** (a) Cubic domain comprised of the (b) 3-D standard unit cell and (c) annular region.

$$V_{ice} = V_{water} \frac{\rho_{water}}{\rho_{ice}} \quad (15)$$

When performing the renormalization process, the change in dimensions of the renormalized block is taken into consideration as ETC is an intensive property, while resistance is extensive (Huang & Fan, 2005).

### 4.3. Postprocessing

Given that the LB simulation is required to be performed on a cubic domain and the renormalization process on  $(2^n)^3$  blocks (Huang & Fan, 2005), we calculated ETC of the cubic domain ( $\bar{k}_{Cube}$ ) comprised of the 3-D standard unit cell and an annular region (see Figure 4) and used weighted averaging method to obtain ETC of the unit cell ( $\bar{k}_{Cell}$ ), as illustrated in Equation 16. Note that the annular region essentially contains gas.

$$\bar{k}_{Cell} = \frac{\bar{k}_{Cube} V_{Cube} - k_{N_2} V_{Ann.}}{V_{Cell}} \quad (16)$$

where  $V$  is the volume.

## 5. Results and Discussion

In this section, we present the experimental results along with the numerical model predictions. Moreover, we plotted our model predictions together with a number of existing models in the literature against the experimental results. This helps us to understand the accuracy of the newly developed model in comparison with the other models.

### 5.1. Experimental Results

#### 5.1.1. Dependence on Overburden and Pore Pressures

Figure 5 shows the measured ETC of partially saturated sediment samples (12.6 wt.%) against the effective overburden pressure at three different pore pressures and a constant temperature (0.5°C). General trends at different pore pressures have been also added to assist with when discussing the thermal conduction characteristics. As expected, increasing the effective overburden pressure results in a higher ETC. This could be attributed to two main factors. The first is the higher particle-particle conduction through the contact area (lower TCR). Increasing the effective overburden pressure results in a higher contact area, as can be simply confirmed by Hertz contact equation (the inset in Figure 5). Given the intrinsic thermal conductivity of sand particles is considerably higher than that of the other constituents, a lower TCR and greater contribution from the particle-particle conduction to ETC is expected when the effective overburden pressure increases. This contribution essentially depends on the contact area, hence more influential at lower effective overburden pressure values. Increasing the effective overburden pressure may also increase the coordination number, which results in a higher number of particles in contact with the particle under consideration. The other factor to be considered is the higher particle-fluid-particle conduction. Increasing the effective overburden pressure results in redistribution of pore fluids enclosing the contact area. Assuming the

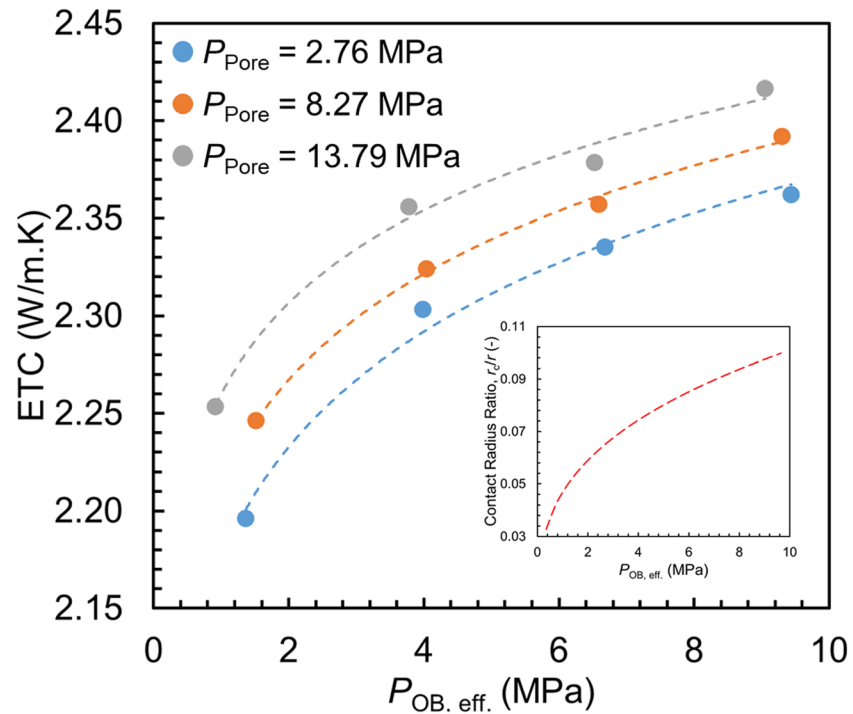


**Figure 5.** ETC versus the effective overburden pressure ( $P_{OB, eff.}$ ) at three different pore pressures ( $P_{Pore}$ );  $T = 0.5^{\circ}\text{C}$  and  $\theta_w = 12.6$  wt.%. Contact radius ratio is also plotted according to Hertz contact equation against the effective overburden pressure as an inset.

particles to undergo elastic deformation, when the effective overburden pressure increases, the pore space around the contact areas becomes smaller with a higher capillary pressure. As a consequence, if there is any gas in these regions, it will be displaced by water as the wetting phase. Since these areas contribute critically to the heat transfer, increasing the effective overburden pressure may also facilitate the heat conduction through these critical pathways.

As can also be seen in Figure 5, ETC is directly proportional to the pore pressure of the system. Several pore-scale associated heat transfer mechanisms could cause this behavior. The first mechanism could be higher heat conduction and convection in the gas phase. Increasing the pore pressure results in a higher intrinsic thermal conductivity for the gas phase. At  $0.5^{\circ}\text{C}$ , the intrinsic value for the thermal conductivity of  $\text{N}_2$  at 13.79 MPa is around 24% higher than 2.76 MPa. Apart from that, higher pore pressure can improve the convective heat transfer mechanism in the gas phase. The other mechanism is higher heat transfer at the fluid-fluid interface. In a multiphase system, increasing the pore pressure enhances the mass transfer at the fluid-fluid interface. This mass transfer is always associated with an energy transfer. Therefore, it is expected to have more contribution in the heat transfer from the gas-water interface at elevated pore pressures. The other interesting mechanism could be the redistribution of the water toward the smaller pores. Since gas is the nonwetting phase in the system, it prefers to occupy the largest pores whereby influencing the pore water network. In fact, when pore pressure increases, gas pushes water from the large pores to the small ones where the capillary pressure is higher. These small pores remarkably contribute to the heat transfer; hence, the presence of water with higher thermal conductivity in these pores is conducive toward higher ETC.

### 5.1.2. Dependence on Temperature and Overburden Pressure

Figure 6 illustrates the measured ETC of partially saturated sediment samples (12.6 wt.%) against the effective overburden pressure at different temperatures and constant pore pressure (3.45 MPa). As observed, the increase in the effective overburden pressure at both unfrozen and frozen conditions resulted in a higher ETC. Potential influential mechanisms are already discussed in section 5.1.1.

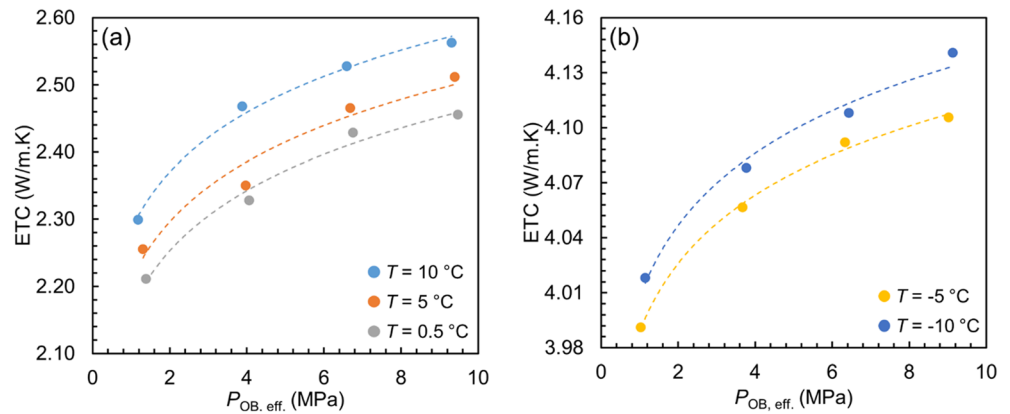


**Figure 6.** ETC versus the effective overburden pressure ( $P_{OB, \text{eff.}}$ ) at (a) unfrozen conditions and (b) frozen conditions;  $P_{\text{Pore}} = 3.45$  MPa and  $\theta_w = 12.6$  wt.%.

ETC values measured at frozen conditions are markedly higher in comparison with unfrozen conditions since on one hand the intrinsic thermal conductivity of ice is almost 4 times more than that of water and on the other hand the transformation of water to ice is associated with volume expansion in the water phase. Our measurements show that the transformation of water to ice resulted in the gas volumetric saturation ( $S_g$ ) to decrease around 7% relative to its initial value. Hence, the results are presented in Figure 6 separately, according to the thermal state of the system, to allow for a clearer investigation.

Increasing the system temperature at unfrozen conditions results in a higher ETC (Figure 6a). This could be due to higher heat conduction and convection in the pore fluids. The intrinsic thermal conductivity of each constituent is directly proportional to the system temperature at the temperature range we dealt with. Therefore, a higher temperature may increase the contribution of heat conduction from each component in ETC. At 3.45 MPa, the intrinsic value for the thermal conductivity of  $N_2$  at 10°C is not significantly different from 0.5°C. However, despite the pore pressure, temperature change also can influence the intrinsic thermal conductivity of water and sand particles. Increasing the system temperature could also improve the convective heat transfer mechanism in the pore fluids (i.e., gas and water), resulting in a higher ETC. The other factor that could play a role is the higher heat transfer at the fluid-fluid interface. Similar to what discussed earlier for the effect of the pore pressure, increasing the system temperature results in a higher mass and energy transfer in the gas-water interface and higher ETC, accordingly.

As shown in Figure 6b, further reducing the system temperature at frozen conditions resulted in a higher ETC, a behavior against what is observed at unfrozen conditions. This behavior could be attributed to the presence of unfrozen water at the critical pathways. It has been shown that the unfrozen water content at  $-5^\circ\text{C}$  is higher than  $-10^\circ\text{C}$  (Istomin et al., 2017). This unfrozen water with a significantly lower thermal conductivity than ice still contributes critically to the heat transfer because ice formation starts at larger pores first and pore fluid migrates toward the nucleating ice due to cryosuction (Hohmann, 1997). Therefore, at  $-5^\circ\text{C}$ , ETC is more influenced by the unfrozen water content. It should also be noted that the transformation of unfrozen water to ice could result in further volume expansion and contribution in ETC. Moreover, heat conduction in ice is higher at lower temperatures. It has been shown that the intrinsic thermal conductivity of ice is negatively correlated with temperature (Slack, 1980). Therefore, it could be expected that the ice contribution in the heat transfer would be higher at  $-10^\circ\text{C}$  relative to  $-5^\circ\text{C}$ , resulting in a higher ETC.

As observed in Figure 6, enhancement of ETC as a result of increasing the effective overburden pressure is typically smaller at frozen conditions compared with unfrozen conditions. The average enhancement rates of ETC at unfrozen and frozen conditions are  $\sim 0.0316$  and  $0.0146$  W/(m.K.MPa), respectively. This behavior could be due to the fact that at frozen conditions, ice crystals could act as coarse grains pushing apart the sediment grains, hence enlarging the sediment pores, a phenomenon known as ice-forced heave, and eventually influence ETC negatively. A similar phenomenon caused by gas hydrates has been already observed to be markedly influential in permeation characteristics of hydrate-bearing sediments (Okwananke et al., 2019). Moreover, it can be seen that ETC enhancement is higher for an individual effective overburden pressure at

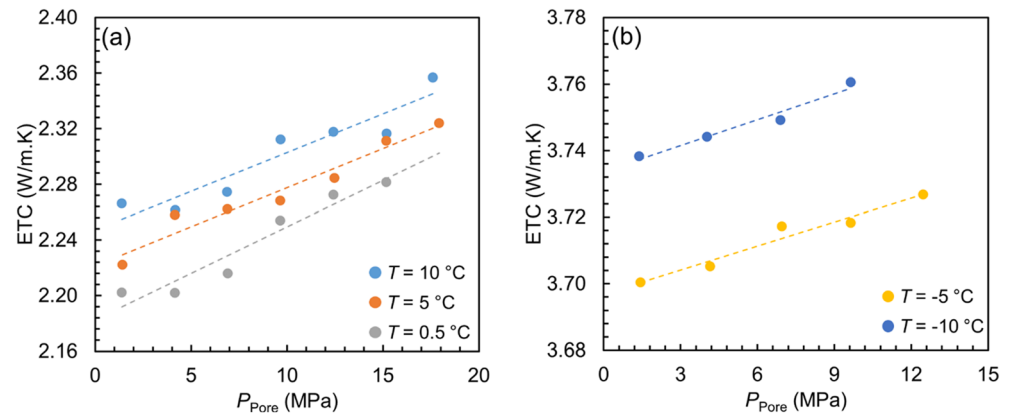


**Figure 7.** ETC versus the pore pressure ( $P_{\text{Pore}}$ ) at (a) unfrozen conditions and (b) frozen conditions;  $P_{\text{OB, eff}} = 3.45$  MPa and  $\theta_w = 12.6$  wt.%.

unfrozen conditions. This behavior can clearly highlight the contribution of the heat conduction and convection in the pore fluids along with the heat transfer at the fluid-fluid interface in ETC at unfrozen conditions.

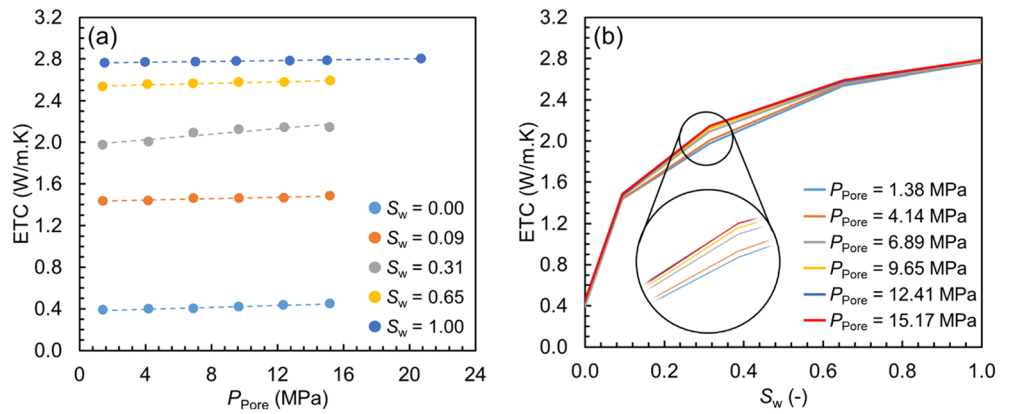
### 5.1.3. Dependence on Temperature and Pore Pressure

Figure 7 shows the measured ETC of partially saturated sediment samples (12.6 wt.%) against the pore pressure at different temperatures and a constant effective overburden pressure (3.45 MPa). As expected, ETC increases as the pore pressure increases for both unfrozen and frozen sediments. We already discussed potential influential mechanisms in section 5.1.1. Dependence on the system temperature is also observed to be similar to what discussed in section 5.1.2. Here, the contribution of the heat conduction and convection in the pore fluids in conjunction with the heat transfer at the fluid-fluid interface to ETC is observed once again to be more influential at unfrozen conditions. We should note that care was taken not to be within the hydrate phase boundary of  $\text{N}_2$  when performing the ETC measurements. Hence, it is observed that the ETC measurement was only conducted outside  $\text{N}_2$  hydrate stability zones at both unfrozen and frozen conditions.

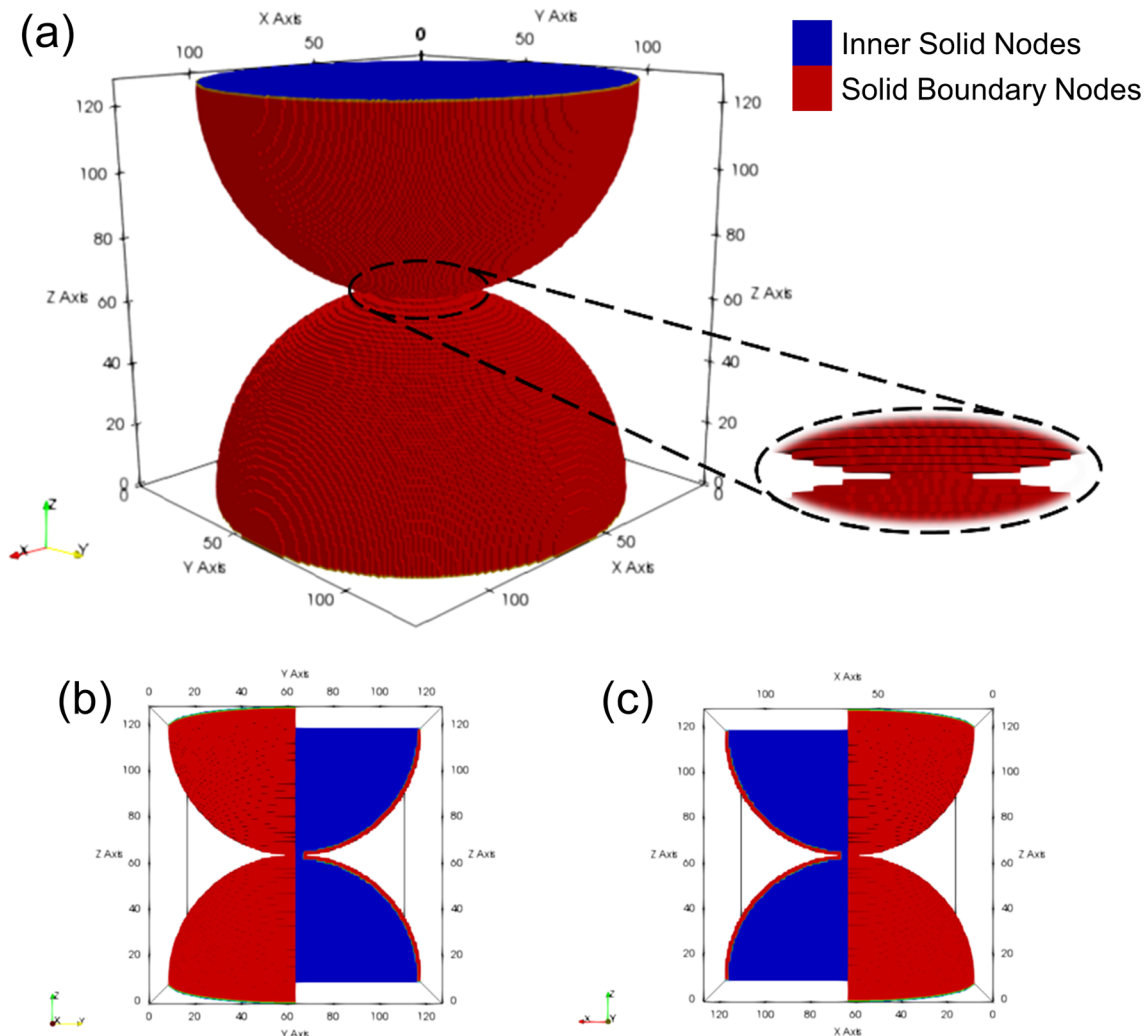
### 5.1.4. Dependence on Water Content

Figure 8 illustrates ETC of partially saturated sediment samples against the pore pressure and volumetric water saturation ( $S_w$ ) at a constant temperature (0.5°C) and effective overburden pressure (3.45 MPa). According to Figure 8a, ETC could be positively correlated with the pore pressure, which can be interpreted in the similar mechanisms previously discussed in section 5.1.1. We should also note that for fully saturated sediments we carried out the ETC measurements for more elevated pore pressures up to 20.68 MPa since water is incompressible and injection of a small amount of water could result in a drastic increase in the pore pressure.

Figure 8b enables us for further investigation regarding the effect of the water content on ETC. At a typical pore pressure, it can be seen that ETC increases considerably once the sediment experiences a small increase in the water content, gaining almost 45% of the heat transfer capability at fully saturated conditions during wetting from dry state to around 10% volumetric water saturation. This rapid increase in ETC is because the sediment experiences the pendular regime at which water forms a thin film around sediment particles and builds water bridges at the contacts, which results in a significant improvement in the connectivity of heat transfer pathways throughout the system (Dong et al., 2015). In fact, our sediment samples had very limited hydration stage at the early stage of wetting, as there was no fines content (clay and silt) in the system (Dong et al., 2015). This behavior is in accordance with the correlation proposed for the critical water content ( $\theta_c$ ) as a function of the clay content by Sadeghi et al. (2018). According to Figure 8b, the pendular regime for our sediment samples is ranging from  $S_w = 0$  to 15%. At higher saturations (up to 70%), prevalence of the funicular regime is observed where ETC still increases gradually mainly due to the buildup of the pore water network. The effect of the pore pressure on ETC can also be observed to be more obvious at this stage given that the establishment of the pore water network is influenced by the pore pressure of the system, as



**Figure 8.** ETC versus the (a) pore pressure ( $P_{\text{Pore}}$ ) at different volumetric water saturations and (b) volumetric water saturation ( $S_w$ ) at different pore pressures;  $T = 0.5^\circ\text{C}$  and  $P_{\text{OB, eff.}} = 3.45 \text{ MPa}$ .



**Figure 9.** Discretized cubic domain: (a) 3-D view, (b) view perpendicular to x axis, and (c) view perpendicular to y axis. The solid boundary nodes (red) that are in contact with fluid are treated differently from the inner solid nodes (blue) to eliminate unnecessary computations.

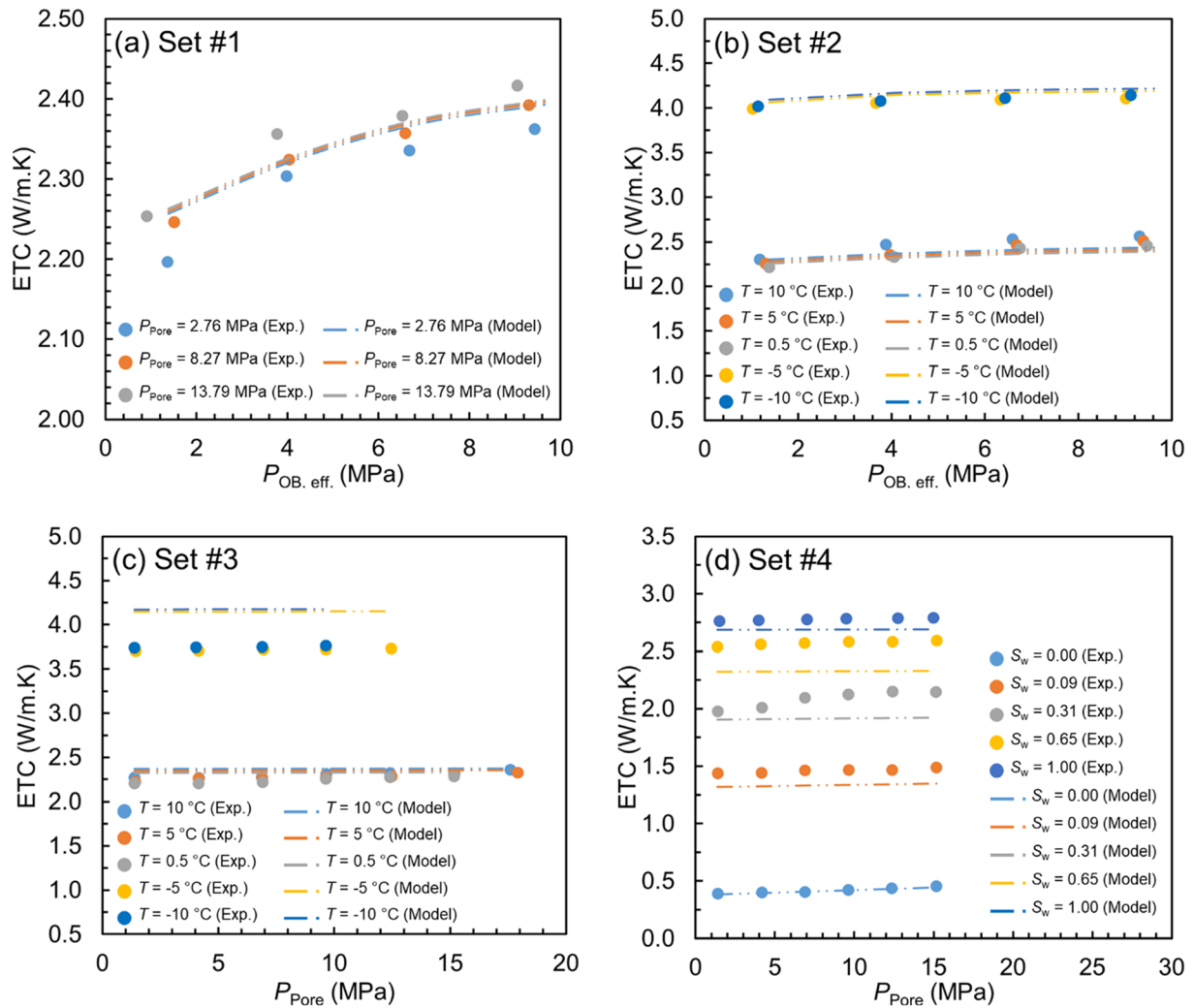


**Figure 10.** Measured and predicted ETC values versus (a) the effective overburden pressure at different pore pressures,  $T = 0.5^\circ\text{C}$  and  $\theta_w = 12.6$  wt.% (Set #1), (b) the effective overburden pressure at different temperatures,  $P_{\text{Pore}} = 3.45$  MPa and  $\theta_w = 12.6$  wt.% (Set #2), (c) the pore pressure at different temperatures,  $P_{\text{OB, eff.}} = 3.45$  MPa and  $\theta_w = 12.6$  wt.% (Set #3), and (d) the pore pressure at different volumetric water saturations,  $T = 0.5^\circ\text{C}$  and  $P_{\text{OB, eff.}} = 3.45$  MPa (Set #4).

discussed in section 5.1.1. At saturations higher than 70%, the sediment experiences the capillary regime at which the effect of the water content on ETC becomes relatively inconspicuous as increasing the water content does not alter the preferred heat flow pathways or their connectivity anymore.

### 5.2. Numerical Model Predictions

Figure 9 visualizes the cubic domain comprised of the standard unit cell and annular region. The optimum resolution of the numerical model, that is, the optimum renormalization rank in terms of the stabilization of the results and computational cost, was found to be  $2^7$  via running the model and processing the simulation results at five different resolutions ( $2^5$ ,  $2^6$ ,  $2^7$ ,  $2^8$ , and  $2^9$ ). This means that the model is required to undergo seven stages of the renormalization process to obtain corresponding ETC. Further details regarding the procedure followed to choose the optimum resolution could be found in the supporting information.

As mentioned earlier, the unit cell contains two monosized touching hemispheres. The contact region set for the effective overburden pressure of 3.45 MPa is also shown in Figure 9a. It should be noted that the number of nodes in the contact region was determined according to the contact radius ratio ( $r_c/r$ ) with respect to the desired effective overburden pressure. Moreover, it can be seen that the solid boundary nodes (which lie at



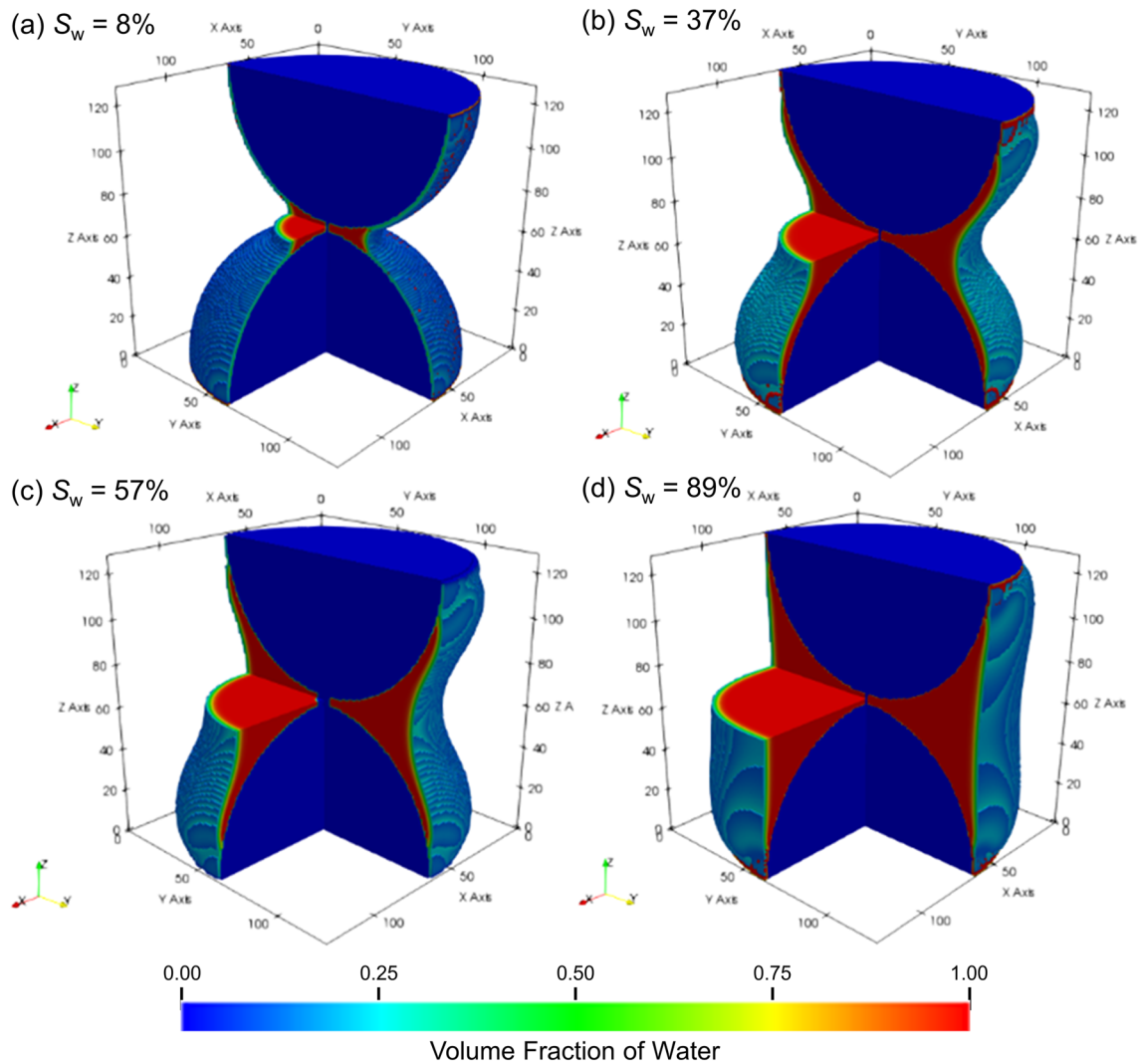


**Figure 11.** Water distribution at the equilibrium conditions in the cubic domain at volumetric saturations of (a) 8%, (b), 37%, (c) 57%, and (d) 89%. The rest of the cell (white space) is occupied by the gas phase.

the solid-fluid interface) are visualized in red, a different color from the inner solid nodes (which are isolated hence inactive), as the boundary nodes should be treated differently in terms of the boundary conditions in the preprocessing step (the LB simulation) to eliminate unnecessary computations at inactive nodes (Sukop & Thorne, 2006). The no-slip boundary conditions were imposed for the outer walls of the domain ( $x$ ,  $y$ , and  $z$  directions) by using the standard bounce-back method. Bounce-back boundaries with a controllable contact angle were also considered for the solid boundary nodes. Figures 9b and 9c also visualize the cubic domain from two different views, perpendicular to  $x$  and  $y$  axes, respectively. The porosity of the standard unit cell can be approximately obtained as 33%, which is quite close to the porosity of our sediment samples ranging in 38–40%.

The model was run to predict ETC with respect to the system temperature, pore pressure, effective overburden pressure, and water content at which we measured ETC. The predicted values are presented in Figure 10

in comparison with the experimental data. As could be seen, the model adequately accounts for the effect of temperature, pore pressure, overburden pressure, and water content when predicting ETC. Snapshots taken from the distribution of water at different saturations in equilibrium with gas are also presented in Figure 11 to help further explore how the model is able to capture pore-scale

**Table 3**  
Average Relative Deviations of the Model Predictions From Experimental Data

Experimental set	Set #1	Set #2	Set #3	Set #4
ARD (%)	0.86	2.28	5.94	6.08

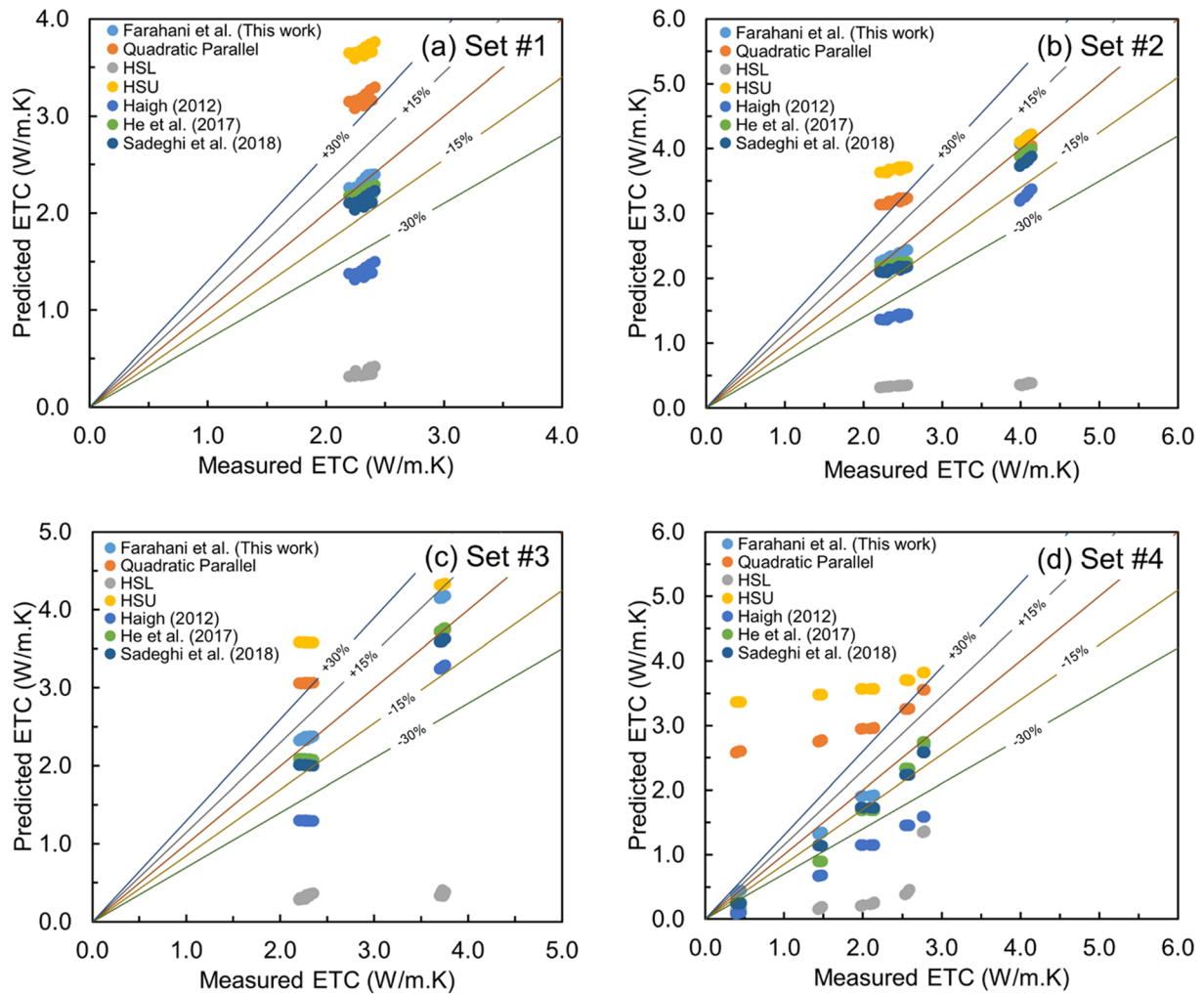


Figure 12. Comparison of the predicted ETC values using different models with the experimental data.

mechanisms in predicting ETC. As observed, the model is able to consider the heat conduction through the particle-particle contact area specified according to the Hertz contact equation. Next, the particle-fluid-particle conduction is well taken into consideration, particularly at low water saturations (Figure 11a) where water as the wetting phase forms a thin film on the particles and builds capillary bridges enclosing the contacts, contributing significantly to the improvement of ETC. As discussed in section 5.1.1, the intrinsic thermal conductivity of the gas phase ( $N_2$ ) is a function of the pressure, enabling the model to account for the effect of the pore pressure on ETC. Moreover, the fluid-fluid interfacial phenomena are accommodated at the preprocessing step where the volume fraction of water at the interface is determined via applying free-energy LBM. Average relative deviations (ARD) were also calculated using Equation 17 and provided in Table 3, evidencing an excellent agreement between the model predictions and experimental data.

$$ARD (\%) = \frac{100}{n} \sum_{i=1}^n \left| \frac{ETC_{Model, i} - ETC_{Exp, i}}{ETC_{Exp, i}} \right| \quad (17)$$

At frozen conditions (Figures 10b and 10c), it is observed that the model predictions are all higher than the experimental data. This

Table 4  
Summary of RMSE Analysis

No.	Model	Experimental sets			
		Set #1	Set #2	Set #3	Set #4
1	Farahani et al. (this work)	0.011	0.026	0.071	0.071
2	Quadratic parallel	0.371	0.258	0.288	2.395
3	HSL	0.849	0.879	0.873	0.769
4	HSU	0.582	0.415	0.487	3.267
5	Haigh (2012)	0.397	0.343	0.364	0.544
6	He et al. (2017)	0.057	0.068	0.071	0.258
7	Sadeghi et al. (2018)	0.087	0.096	0.101	0.236

could be due to the procedure we followed to accommodate the transformation of water to ice in the processing step. In fact, the model neglects the unfrozen water content, which may critically contribute to ETC, and calculates the amount of the volume expansion according to Equation 15. Ice-forced heave is the other possible factor required to be further investigated experimentally.

We also compared the predictions with those of six existing models: Quadratic Parallel (Dong et al., 2015), Hashin-Shtrikman Lower Bound (HSL) (Dong et al., 2015), Hashin-Shtrikman Upper Bound (HSU) (Dong et al., 2015), Haigh (2012), He et al. (2017), and Sadeghi et al. (2018). When using these models to predict ETC, the instantaneous porosity and water saturation corresponding to each experimental data point were considered. Moreover, the volume expansion due to the transformation of water to ice was included when predicting ETC at frozen conditions. Figure 12 exhibits the comparison of the different modeling predictions of ETC with the experimental data. As expected, all predictions are within the Hashin-Shtrikman bounds. It can be seen that the other models except HSU and quadratic parallel underestimate ETC; some even fail to make predictions with a relative error of less than 30%. This could be due to the fact that the predictive models proposed so far are mixing models relying on simple mixing laws such as series, parallel, and quadratic parallel models, empirical models strongly depending on the experimental data such as the model developed by He et al. (2017), or mathematical models that were implicitly/explicitly developed such as Hashin-Shtrikman's model, Haigh model (Haigh, 2012), and GD model (Ghanbarian & Daigle, 2016) and its explicit form developed by Sadeghi et al. (2018). Therefore, they would not be able to capture all complex pore-scale associated phenomena contributing to ETC. Table 4 provides root-mean-square error (RMSE) for each predictive model, calculated using Equation 18. As observed, RMSE values for our pore-scale numerical model are less than 0.1 W/m.K, significantly lower than those of the other predictive models, confirming its accuracy and reliability.

$$RMSE = \sqrt{\frac{\sum_{i=1}^n (ETC_{Model, i} - ETC_{Exp, i})^2}{n}} \quad (18)$$

## 6. Conclusion

In this work, we conducted a mechanistic study on the heat transfer in partially saturated sediments at unfrozen and frozen conditions. Four sets of experiment were carried out, and the effects of a variety of parameters on heat transfer mechanisms were investigated, including pore pressure, overburden pressure, temperature, and degree of water/ice saturation. A pore-scale numerical model was also developed based on the deployment of free-energy LBM and a space renormalization method for the prediction of ETC. The model prediction is in good agreement with the experimental data with an average RMSE of less than 0.1 W/m.K. The experimental and modeling results reveal that the heat transfer in porous media is complex phenomena and controlled by several key factors.

1. Heat transfer in porous media is largely affected by water content, packing structure, and wettability characteristics of grains as they influence the capillary pressure and preferential occupancy and hence the water distribution in pores.
2. Coordination number and physical contact among sediment particles substantially affect the heat transfer. In fact, ETC is remarkably influenced by the particle-particle conduction through the contact regions. The particle-fluid-particle conduction through the pathways enclosing the contact regions is the next important heat transfer mechanism which contributes to ETC, particularly at low water saturations.
3. Heat conduction and convection in the pore fluids should be taken into account to further improve the model performance, especially at elevated pore pressures and temperatures.
4. ETC at frozen conditions was affected by the unfrozen water content still enclosing the contact regions. Ice-forced heave may also play a role in heat transfer at frozen condition. However, this phenomenon is to be further investigated.
5. Performance of the pore-scale model could be further improved for different packing structures such as body centered cubic and face centered cubic, which requires employing different contact equations appropriate with the packing structure and contact angles, and by coupled discrete element method-computational fluid dynamics methods. Such coupled methods could also assist with when investigating the effect of particle shape and size distribution. More accurate predictions could be

achieved at frozen conditions by accounting for the coexistence of ice and unfrozen water together with their pore-scale distribution and interfacial effects. This is of particular importance at subzero temperatures in the vicinity of the freezing point where the amount of unfrozen water is not negligible, and the ice crystals are floating in unfrozen water (pore-filling habit).

### Conflict of Interest

The authors declare no financial conflict of interest.

### Data Availability Statement

The experimental data and model predictions are available at Mendeley Data (<https://doi.org/10.17632/zrd74wtvpx.2>).

### Acknowledgments

The authors would gratefully acknowledge Heriot-Watt University for providing the PhD funding for Mehrdad Vasheghani Farahani through James Watt Scholarship.

### References

- Abdel-Wahed, R. M., Pfender, E., & Eckert, E. R. G. (1978). A transient method for measuring thermal properties of soils. *Wärme- und Stoffübertragung*, *11*(1), 1–8. <https://doi.org/10.1007/BF01881514>
- Abdulagatova, Z., Abdulagatov, I. M., & Emirov, V. N. (2009). Effect of temperature and pressure on the thermal conductivity of sandstone. *International Journal of Rock Mechanics and Mining Sciences*, *46*(6), 1055–1071. <https://doi.org/10.1016/j.ijrmms.2009.04.011>
- Abuel-Naga, H. M., Bergado, D. T., & Bouazza, A. (2008). Thermal conductivity evolution of saturated clay under consolidation process. *International Journal of Geomechanics*, *8*(2), 114–122. [https://doi.org/10.1061/\(ASCE\)1532-3641\(2008\)8:2\(114\)](https://doi.org/10.1061/(ASCE)1532-3641(2008)8:2(114))
- Abuel-Naga, H. M., Bergado, D. T., Bouazza, A., & Pender, M. J. (2009). Thermal conductivity of soft Bangkok clay from laboratory and field measurements. *Engineering Geology*, *105*(3–4), 211–219. <https://doi.org/10.1016/j.enggeo.2009.02.008>
- ASTM D5334-14 (2014). Standard test method for determination of thermal conductivity of soil and soft rock by thermal needle probe procedure. West Conshohocken, PA: ASTM International. <https://doi.org/10.1520/D5334-14>
- Bahrami, M., Yovanovich, M. M., & Culham, J. R. (2006). Effective thermal conductivity of rough spherical packed beds. *International Journal of Heat and Mass Transfer*, *49*(19–20), 3691–3701. <https://doi.org/10.1016/j.ijheatmasstransfer.2006.02.021>
- Bakhshian, S., Hosseini, S. A., & Shokri, N. (2019). Pore-scale characteristics of multiphase flow in heterogeneous porous media using the lattice Boltzmann method. *Scientific Reports*, *9*(1), 3377. <https://doi.org/10.1038/s41598-019-39741-x>
- Bakhshian, S., & Sahimi, M. (2016). Computer simulation of the effect of deformation on the morphology and flow properties of porous media. *Physical Review E*, *94*(4), 42903. <https://doi.org/10.1103/PhysRevE.94.042903>
- Barry-Macaulay, D., Bouazza, A., Singh, R. M., Wang, B., & Ranjith, P. G. (2013). Thermal conductivity of soils and rocks from the Melbourne (Australia) region. *Engineering Geology*, *164*, 131–138. <https://doi.org/10.1016/j.enggeo.2013.06.014>
- Campbell, G. S., Jungbauer, J. D. Jr., Bidlake, W. R., & Hungerford, R. D. (1994). Predicting the effect of temperature on soil thermal conductivity. *Soil Science*, *158*(5), 307–313. <https://doi.org/10.1097/00010694-199411000-00001>
- Chen, S. X. (2008). Thermal conductivity of sands. *Heat and Mass Transfer*, *44*(10), 1241–1246. <https://doi.org/10.1007/s00231-007-0357-1>
- Chen, Y., Valocchi, A. J., Kang, Q., & Viswanathan, H. S. (2019). Inertial effects during the process of supercritical CO<sub>2</sub> displacing brine in a sandstone: Lattice Boltzmann simulations based on the continuum-surface-force and geometrical wetting models. *Water Resources Research*, *55*, 11,144–11,165. <https://doi.org/10.1029/2019WR025746>
- Chu, Z., Zhou, G., Wang, Y., Zhao, X., & Mo, P.-Q. (2019). A supplementary analytical model for the stagnant effective thermal conductivity of low porosity granular geomaterials. *International Journal of Heat and Mass Transfer*, *133*, 994–1007. <https://doi.org/10.1016/j.ijheatmasstransfer.2018.12.167>
- Corasaniti, S., & Gori, F. (2017). Heat conduction in two and three-phase media with solid spherical particles of the same diameter. *International Journal of Thermal Sciences*, *112*, 460–469. <https://doi.org/10.1016/j.ijthermalsci.2016.10.022>
- Cortes, D. D., Martin, A. I., Yun, T. S., Francisca, F. M., Santamarina, J. C., & Ruppel, C. (2009). Thermal conductivity of hydrate-bearing sediments. *Journal of Geophysical Research*, *114*, B11103. <https://doi.org/10.1029/2008JB006235>
- Côté, J., Fillion, M.-H., & Konrad, J.-M. (2011). Estimating hydraulic and thermal conductivities of crushed granite using porosity and equivalent particle size. *Journal of Geotechnical and Geoenvironmental Engineering*, *137*(9), 834–842. [https://doi.org/10.1061/\(ASCE\)GT.1943-5606.0000503](https://doi.org/10.1061/(ASCE)GT.1943-5606.0000503)
- Côté, J., & Konrad, J.-M. (2005). A generalized thermal conductivity model for soils and construction materials. *Canadian Geotechnical Journal*, *42*(2), 443–458. <https://doi.org/10.1139/t04-106>
- Dai, W., Hanaor, D., & Gan, Y. (2019). The effects of packing structure on the effective thermal conductivity of granular media: A grain scale investigation. *International Journal of Thermal Sciences*, *142*, 266–279. <https://doi.org/10.1016/j.ijthermalsci.2019.04.028>
- de Zàrate, J. M. O., Hita, J. L., Khayet, M., & Legido, J. L. (2010). Measurement of the thermal conductivity of clays used in pelotherapy by the multi-current hot-wire technique. *Applied Clay Science*, *50*(3), 423–426. <https://doi.org/10.1016/j.clay.2010.08.012>
- Domine, F., Barrere, M., & Sarrazin, D. (2016). Seasonal evolution of the effective thermal conductivity of the snow and the soil in high Arctic herb tundra at Bylot Island, Canada. *The Cryosphere*, *10*(6), 2573–2588. <https://doi.org/10.5194/tc-10-2573-2016>
- Dong, Y., McCartney, J. S., & Lu, N. (2015). Critical review of thermal conductivity models for unsaturated soils. *Geotechnical and Geological Engineering*, *33*(2), 207–221. <https://doi.org/10.1007/s10706-015-9843-2>
- Du, Y., Li, R., Zhao, L., Yang, C., Wu, T., Hu, G., et al. (2020). Evaluation of 11 soil thermal conductivity schemes for the permafrost region of the central Qinghai-Tibet Plateau. *Catena*, *193*, 104608. <https://doi.org/10.1016/j.catena.2020.104608>
- El Shamy, U., De Leon, O., & Wells, R. (2013). Discrete element method study on effect of shear-induced anisotropy on thermal conductivity of granular soils. *International Journal of Geomechanics*, *13*(1), 57–64. [https://doi.org/10.1061/\(ASCE\)GM.1943-5622.0000165](https://doi.org/10.1061/(ASCE)GM.1943-5622.0000165)
- Ewing, R. P., & Horton, R. (2007). Thermal conductivity of a cubic lattice of spheres with capillary bridges. *Journal of Physics D: Applied Physics*, *40*(16), 4959–4965. <https://doi.org/10.1088/0022-3727/40/16/031>
- Feng, Y. T., Han, K., Li, C. F., & Owen, D. R. J. (2008). Discrete thermal element modelling of heat conduction in particle systems: Basic formulations. *Journal of Computational Physics*, *227*(10), 5072–5089. <https://doi.org/10.1016/j.jcp.2008.01.031>

- Freij-Ayoub, R., Tan, C., Clennell, B., Tohidi, B., & Yang, J. (2007). A wellbore stability model for hydrate bearing sediments. *Journal of Petroleum Science and Engineering*, 57(1-2), 209–220. <https://doi.org/10.1016/j.petrol.2005.10.011>
- Garrett, D., & Ban, H. (2011). Compressive pressure dependent anisotropic effective thermal conductivity of granular beds. *Granular Matter*, 13(5), 685–696. <https://doi.org/10.1007/s10035-011-0273-4>
- Ghanbarian, B., & Daigle, H. (2016). Thermal conductivity in porous media: Percolation-based effective-medium approximation. *Water Resources Research*, 52, 295–314. <https://doi.org/10.1002/2015WR017236>
- Gor, G. Y., Elliot, T. R., & Prévost, J. H. (2013). Effects of thermal stresses on caprock integrity during CO<sub>2</sub> storage. *International Journal of Greenhouse Gas Control*, 12, 300–309. <https://doi.org/10.1016/j.ijggc.2012.11.020>
- Gori, F., & Corasaniti, S. (2013). New model to evaluate the effective thermal conductivity of three-phase soils. *International Communications in Heat and Mass Transfer*, 47, 1–6. <https://doi.org/10.1016/j.icheatmasstransfer.2013.07.004>
- Haigh, S. K. (2012). Thermal conductivity of sands. *Geotechnique*, 62(7), 617–625. <https://doi.org/10.1680/geot.11.P.043>
- Hassanpouryouzband, A., Farahani, M. V., Yang, J., Tohidi, B., Chuvilin, E., Istomin, V., & Bukhanov, B. (2019). Solubility of flue gas or carbon dioxide-nitrogen gas mixtures in water and aqueous solutions of salts: Experimental measurement and thermodynamic modeling. *Industrial and Engineering Chemistry Research*, 58(8), 3377–3394. <https://doi.org/10.1021/acs.iecr.8b04352>
- Hassanpouryouzband, A., Yang, J., Okwananke, A., Burgass, R., Tohidi, B., Chuvilin, E., et al. (2019). An experimental investigation on the kinetics of integrated methane recovery and CO<sub>2</sub> sequestration by injection of flue gas into permafrost methane hydrate reservoirs. *Scientific Reports*, 9(1), 1, 16206–9. <https://doi.org/10.1038/s41598-019-52745-x>
- Hassanpouryouzband, A., Yang, J., Tohidi, B., Chuvilin, E., Istomin, V., & Bukhanov, B. (2019). Geological CO<sub>2</sub> capture and storage with flue gas hydrate formation in frozen and unfrozen sediments: Method development, real time-scale kinetic characteristics, efficiency, and clathrate structural transition. *ACS Sustainable Chemistry & Engineering*, 7(5), 5338–5345. <https://doi.org/10.1021/acssuschemeng.8b06374>
- Hassanpouryouzband, A., Yang, J., Tohidi, B., Chuvilin, E., Istomin, V., Bukhanov, B., & Cheremisin, A. (2018). CO<sub>2</sub> capture by injection of flue gas or CO<sub>2</sub>-N<sub>2</sub> mixtures into hydrate reservoirs: Dependence of CO<sub>2</sub> capture efficiency on gas hydrate reservoir conditions. *Environmental Science and Technology*, 52(7), 4324–4330. <https://doi.org/10.1021/acs.est.7b05784>
- He, H., Dyck, M. F., Horton, R., Ren, T., Bristow, K. L., Lv, J., & Si, B. (2018). Development and application of the heat pulse method for soil physical measurements. *Reviews of Geophysics*, 56(4), 567–620. <https://doi.org/10.1029/2017RG000584>
- He, H., Zhao, Y., Dyck, M. F., Si, B., Jin, H., Lv, J., & Wang, J. (2017). A modified normalized model for predicting effective soil thermal conductivity. *Acta Geotechnica*, 12(6), 1281–1300. <https://doi.org/10.1007/s11440-017-0563-z>
- Hiraiwa, Y., & Kasubuchi, T. (2000). Temperature dependence of thermal conductivity of soil over a wide range of temperature (5–75°C). *European Journal of Soil Science*, 51(2), 211–218. <https://doi.org/10.1046/j.1365-2389.2000.00301.x>
- Hohmann, M. (1997). Soil freezing—The concept of soil water potential. State of the art. *Cold Regions Science and Technology*, 25(2), 101–110. [https://doi.org/10.1016/S0165-232X\(96\)00019-5](https://doi.org/10.1016/S0165-232X(96)00019-5)
- Hovland, M., & Gudmestad, O. T. (2001). Potential influence of gas hydrates on seabed installations. *Natural Gas Hydrates: Occurrence, Distribution, and Detection*. <https://doi.org/10.1029/GM124p0307>
- Huang, D., & Fan, S. (2005). Measuring and modeling thermal conductivity of gas hydrate-bearing sand. *Journal of Geophysical Research*, 110, B01311. <https://doi.org/10.1029/2004JB003314>
- Istomin, V., Chuvilin, E., Bukhanov, B., & Uchida, T. (2017). Pore water content in equilibrium with ice or gas hydrate in sediments. *Cold Regions Science and Technology*, 137, 60–67. <https://doi.org/10.1016/j.coldregions.2017.02.005>
- Johnson, K. L. (1987). *Contact mechanics*. Cambridge, UK: Cambridge University Press. <https://doi.org/10.1017/CBO9781139171731>
- Jongwon, J., Mohammad, J., & Jaehun, A. (2019). Experimental evaluation of the thermal conductivity of silica sands with varying porosity and particle size. *Geotechnical Frontiers*, 2017. <https://doi.org/10.1061/9780784480472.082>
- Kojima, Y., Heitman, J. L., Noborio, K., Ren, T., & Horton, R. (2018). Sensitivity analysis of temperature changes for determining thermal properties of partially frozen soil with a dual probe heat pulse sensor. *Cold Regions Science and Technology*, 151, 188–195. <https://doi.org/10.1016/j.coldregions.2018.03.022>
- Krause, M. J., Avis, S., Dapalo, D., Gaedtker, M., Hafen, N., Haußmann, M., et al. (2019). OpenLB release 1.3: Open source lattice Boltzmann code. Retrieved from <https://www.openlb.net/download>
- Krüger, T., Kusumaatmaja, H., Kuzmin, A., Shardt, O., Silva, G., & Viggien, E. M. (2017). *The lattice Boltzmann method* (Vol. 10). Cham, Switzerland: Springer International Publishing. <https://doi.org/10.1007/978-3-319-44649-3>
- Li, D., Sun, X., & Khaleel, M. (2013). Comparison of different upscaling methods for predicting thermal conductivity of complex heterogeneous materials system: Application on nuclear waste forms. *Metallurgical and Materials Transactions A*, 44(S1), 61–69. <https://doi.org/10.1007/s11661-012-1269-3>
- Likos, W. J. (2015). Pore-scale model for thermal conductivity of unsaturated sand. *Geotechnical and Geological Engineering*, 33(2), 179–192. <https://doi.org/10.1007/s10706-014-9744-9>
- Liu, C. H., Zhou, D., & Wu, H. (2011). Measurement and prediction of temperature effects of thermal conductivity of soils. *Chinese Journal of Geotechnical Engineering*, 33(12), 1877–1886.
- Lu, S., Lu, Y., Peng, W., Ju, Z., & Ren, T. (2019). A generalized relationship between thermal conductivity and matric suction of soils. *Geoderma*, 337, 491–497. <https://doi.org/10.1016/j.geoderma.2018.09.057>
- Lu, S., Ren, T., Gong, Y., & Horton, R. (2007). An improved model for predicting soil thermal conductivity from water content at room temperature. *Soil Science Society of America Journal*, 71(1), 8–14. <https://doi.org/10.2136/sssaj2006.0041>
- Mo, J., & Ban, H. (2017). Measurements and theoretical modeling of effective thermal conductivity of particle beds under compression in air and vacuum. *Case Studies in Thermal Engineering*, 10, 423–433. <https://doi.org/10.1016/j.csite.2017.10.001>
- Nikolaev, I. V., Leong, W. H., & Rosen, M. A. (2013). Experimental investigation of soil thermal conductivity over a wide temperature range. *International Journal of Thermophysics*, 34(6), 1110–1129. <https://doi.org/10.1007/s10765-013-1456-5>
- Norouzi, S., Soleimani, R., Farahani, M. V., & Rasaei, M. R. (2019). *Pore-scale simulation of capillary force effect in water-oil immiscible displacement process in porous media* (Vol. 2019, pp. 1–5). Paper presented at 81st EAGE Conference and Exhibition 2019, European Association of Geoscientists & Engineers. <https://doi.org/10.3997/2214-4609.201900962>
- Okwananke, A., Hassanpouryouzband, A., Vasheghani Farahani, M., Yang, J., Tohidi, B., Chuvilin, E., et al. (2019). Methane recovery from gas hydrate-bearing sediments: An experimental study on the gas permeation characteristics under varying pressure. *Journal of Petroleum Science and Engineering*, 180, 435–444. <https://doi.org/10.1016/j.petrol.2019.05.060>
- Overduin, P. P., Kane, D. L., & van Loon, W. K. P. (2006). Measuring thermal conductivity in freezing and thawing soil using the soil temperature response to heating. *Cold Regions Science and Technology*, 45(1), 8–22. <https://doi.org/10.1016/j.coldregions.2005.12.003>

- Pinheiro, A. S., Da Costa, Z. M., Bell, M. J. V., Anjos, V., Dantas, N. O., & Reis, S. T. (2011). Thermal characterization of iron phosphate glasses for nuclear waste disposal. *Optical Materials*, 33(12), 1975–1979. <https://doi.org/10.1016/j.optmat.2011.03.050>
- Putkonen, J. (2003). Determination of frozen soil thermal properties by heated needle probe. *Permafrost and Periglacial Processes*, 14(4), 343–347. <https://doi.org/10.1002/ppp.465>
- Sadeghi, M., Ghanbarian, B., & Horton, R. (2018). Derivation of an explicit form of the percolation-based effective-medium approximation for thermal conductivity of partially saturated soils. *Water Resources Research*, 54, 1389–1399. <https://doi.org/10.1002/2017WR021714>
- Sadullah, M. S., Semprebon, C., & Kusumaatmaja, H. (2018). Drop dynamics on liquid-infused surfaces: The role of the lubricant ridge. *Langmuir*, 34(27), 8112–8118. <https://doi.org/10.1021/acs.langmuir.8b01660>
- Semprebon, C., Krüger, T., & Kusumaatmaja, H. (2016). Ternary free-energy lattice Boltzmann model with tunable surface tensions and contact angles. *Physical Review E*, 93(3), 33305. <https://doi.org/10.1103/PhysRevE.93.033305>
- Siu, W. W. M., & Lee, S. H.-K. (2000). Effective conductivity computation of a packed bed using constriction resistance and contact angle effects. *International Journal of Heat and Mass Transfer*, 43(21), 3917–3924. [https://doi.org/10.1016/S0017-9310\(00\)00051-X](https://doi.org/10.1016/S0017-9310(00)00051-X)
- Slack, G. A. (1980). Thermal conductivity of ice. *Physical Review B*, 22(6), 3065–3071. <https://doi.org/10.1103/PhysRevB.22.3065>
- Slavin, A. J., Londry, F. A., & Harrison, J. (2000). A new model for the effective thermal conductivity of packed beds of solid spheroids: Alumina in helium between 100 and 500°C. *International Journal of Heat and Mass Transfer*, 43(12), 2059–2073. [https://doi.org/10.1016/S0017-9310\(99\)00290-2](https://doi.org/10.1016/S0017-9310(99)00290-2)
- Sukop, M. C., & Thorne, D. T. (2006). *Lattice Boltzmann modeling*. Berlin, Heidelberg: Springer-Verlag. <https://doi.org/10.1007/978-3-540-27982-2>
- Tarnawski, V. R., Momose, T., & Leong, W. H. (2009). Assessing the impact of quartz content on the prediction of soil thermal conductivity. *Geotechnique*, 59(4), 331–338. <https://doi.org/10.1680/geot.2009.59.4.331>
- van Antwerpen, W., du Toit, C. G., & Rousseau, P. G. (2010). A review of correlations to model the packing structure and effective thermal conductivity in packed beds of mono-sized spherical particles. *Nuclear Engineering and Design*, 240(7), 1803–1818. <https://doi.org/10.1016/j.nucengdes.2010.03.009>
- Vasheghani Farahani, M., Foroughi, S., Norouzi, S., & Jamshidi, S. (2019). Mechanistic study of fines migration in porous media using lattice Boltzmann method coupled with rigid body physics engine. *Journal of Energy Resources Technology*, 141(12). <https://doi.org/10.1115/1.4044976>
- Venuleo, S., Laloui, L., Terzis, D., Hueckel, T., & Hassan, M. (2016). Microbially induced calcite precipitation effect on soil thermal conductivity. *Géotechnique Letters*, 6(1), 39–44. <https://doi.org/10.1680/jgele.15.00125>
- Vora, H. B., & Dugan, B. (2019). Porosity-permeability relationships in mudstone from pore-scale fluid flow simulations using the lattice Boltzmann method. *Water Resources Research*, 55, 7060–7071. <https://doi.org/10.1029/2019WR024985>
- Waite, W. F., Santamarina, J. C., Cortes, D. D., Dugan, B., Espinoza, D. N., Germaine, J., et al. (2009). Physical properties of hydrate-bearing sediments. *Reviews of Geophysics*, 47, RG4003. <https://doi.org/10.1029/2008RG000279>
- Wang, X., Wang, Z., Deng, X., Sun, B., Zhao, Y., & Fu, W. (2017). Coupled thermal model of wellbore and permafrost in Arctic regions. *Applied Thermal Engineering*, 123, 1291–1299. <https://doi.org/10.1016/j.applthermaleng.2017.05.186>
- Weidenfeld, G., Weiss, Y., & Kalman, H. (2004). A theoretical model for effective thermal conductivity (ETC) of particulate beds under compression. *Granular Matter*, 6(2-3), 121–129. <https://doi.org/10.1007/s10035-004-0170-1>
- Wöhrwag, M., Semprebon, C., Mazloomi Moqaddam, A., Karlin, I., & Kusumaatmaja, H. (2018). Ternary free-energy entropic lattice Boltzmann model with a high density ratio. *Physical Review Letters*, 120(23), 234501. <https://doi.org/10.1103/PhysRevLett.120.234501>
- Yu, X., Zhang, N., Pradhan, A., & Puppala, A. J. (2016). Thermal conductivity of sand–kaolin clay mixtures. *Environmental Geotechnics*, 3(4), 190–202. <https://doi.org/10.1680/jenge.15.00022>
- Yun, T. S., & Evans, T. M. (2010). Three-dimensional random network model for thermal conductivity in particulate materials. *Computers and Geotechnics*, 37(7-8), 991–998. <https://doi.org/10.1016/j.compgeo.2010.08.007>
- Yun, T. S., & Santamarina, J. C. (2007). Fundamental study of thermal conduction in dry soils. *Granular Matter*, 10(3), 197–207. <https://doi.org/10.1007/s10035-007-0051-5>
- Zhang, L., Zhang, C., Zhang, K., Zhang, L., Yao, J., Sun, H., & Yang, Y. (2019). Pore-scale investigation of methane hydrate dissociation using the lattice Boltzmann method. *Water Resources Research*, 55, 8422–8444. <https://doi.org/10.1029/2019WR025195>
- Zhang, N., & Wang, Z. (2017). Review of soil thermal conductivity and predictive models. *International Journal of Thermal Sciences*, 117, 172–183. <https://doi.org/10.1016/j.ijthermalsci.2017.03.013>
- Zhang, N., Yu, X., Pradhan, A., & Puppala, A. J. (2015). Thermal conductivity of quartz sands by thermo-time domain reflectometry probe and model prediction. *Journal of Materials in Civil Engineering*, 27(12). [https://doi.org/10.1061/\(ASCE\)MT.1943-5533.0001332](https://doi.org/10.1061/(ASCE)MT.1943-5533.0001332)
- Zhao, Y., & Si, B. (2019). Thermal properties of sandy and peat soils under unfrozen and frozen conditions. *Soil and Tillage Research*, 189, 64–72. <https://doi.org/10.1016/j.still.2018.12.026>
- Zhao, Y., Si, B., Zhang, Z., Li, M., He, H., & Hill, R. L. (2019). A new thermal conductivity model for sandy and peat soils. *Agricultural and Forest Meteorology*, 274, 95–105. <https://doi.org/10.1016/j.agrformet.2019.04.004>
- Zhou, J., Yu, A., & Zhang, Y. (2007). A boundary element method for evaluation of the effective thermal conductivity of packed beds. *Journal of Heat Transfer*, 129(3), 363–371. <https://doi.org/10.1115/1.2430721>